THESIS FOR THE DEGREE OF LICENTIATE OF ENGINEERING

Filtration of Cellulosic Materials

The impact of ionic strength and electric field

ANNA LIDÉN

Department of Chemistry and Chemical Engineering

CHALMERS UNIVERSITY OF TECHNOLOGY

Gothenburg, Sweden 2021

Filtration of Cellulosic Materials
The impact of ionic strength and electric field
ANNA LIDÉN

Technical report no 2021:13

Department of Chemistry and Chemical Engineering
Chalmers University of Technology
SE-412 96 Gothenburg
Sweden
Telephone + 46 (0)31-772 1000

Cover: Art by Isa Bengzon

Printed by Chalmers Reproservice
Gothenburg, Sweden 2021

Filtration of Cellulosic Materials
The impact of ionic strength and electric field
ANNA LIDÉN
Department of Chemistry and Chemical Engineering
Chalmers University of Technology

Abstract

It is crucial that dewatering technology is considered if an economically feasible production of cellulosic materials is to be achieved. Cellulosic materials are often produced in dilute streams and therefore require great amounts of water to be removed to allow for reasonable transportation costs and/or further modifications. Although various types of drying techniques are suitable for this purpose, they are rather energy intensive. One way of reducing the total energy demand is to add an efficient mechanical dewatering step prior to the drying step: filtration is the technique most commonly used. However, micro/nano cellulosic materials have large surface areas, resulting in an extensive filtration resistance and thus requiring large filters. It therefore becomes important to evaluate the impact of external factors, and ionic strength in particular, as this is known to affect electrostatic interactions between cellulose particles and may thereby impact the filtration behaviour. Another alternative is to use an electro-assisted method where an electric field, applied across the filter chamber, introduces several electrokinetic phenomena that can be beneficial to dewatering.

The work presented in this thesis examines the filtration of cellulosic material in the form of microcrystalline cellulose (MCC) and microfibrillated cellulose (MFC). The influence of ionic strength on the dead-end filtration of MCC was investigated by the addition of NaCl in the range of 0-1 g/L. It was concluded that increasing the ionic strength improved the filtration rate: the surface charges of the MCC particles were shielded which, in turn, promoted agglomeration and reduced the total surface area subjected to the liquid flow. This confirms the importance of electrostatic interactions between MCC particles during dead-end filtration.

The MFC was produced via 2,2,6,6-tetramethylpiperidinyl-1-oxyl (TEMPO)-mediated oxidation and an electro-assisted filtration technique was employed to dewater the suspension. Compared to conventional dead-end filtration, electro-assisted filtration significantly improved the dewatering rate due to the electrokinetic phenomena it introduced. Three different levels of electric field were used, and it was observed that the dewatering rate increased proportionally to the strength of the electric field. In addition, molecular dynamic (MD) simulations were performed to obtain an understanding of the dewatering mechanism on a molecular level.

Keywords: dead-end filtration, electro-assisted, ionic strength, microcrystalline cellulose, microfibrillated cellulose

List of publications

The thesis is based on the following appended papers:

Paper I: **Dewatering microcrystalline cellulose: The influence of ionic strength**
Anna Lidén, Nabin Kumar Karna, Tuve Mattsson, Hans Theliander,
Separation and Purification Technology, Volume 264, 2021,
(https://doi.org/10.1016/j.seppur.2020.118245)

Paper II: **Electro-assisted filtration of microfibrillated cellulose: Insights gained from experimental and simulation studies**
Nabin Kumar Karna, Anna Lidén, Jakob Wohlert, Hans Theliander
Submitted Manuscript

Publications not included in the thesis:

Paper I: **Wettability of cellulose surfaces under the influence of an external electric field**
Nabin Kumar Karna, Jakob Wohlert, Anna Lidén, Tuve Mattsson, Hans Theliander,
Journal of Colloid and Interface Science, Volume 589, 2021, Pages 347-355,
(https://doi.org/10.1016/j.jcis.2021.01.003)

Contribution report

Paper I: First author. Planned and performed the filtration experiments together with Nabin Karna. Tuve Mattsson contributed with expertise regarding the filtration set-up. Main responsible for the characterisation. The results were evaluated together with the co-authors. Responsible for drafting the manuscript and revised it after feedback from the co-authors.

Paper II: Shared first author. Main responsible for planning and conducting the experimental work. Nabin Karna was responsible for the molecular dynamic simulations. The results were discussed with the co-authors. The manuscript was prepared together with Nabin Karna.

1 Introduction 1
1.1 Objectives 3
1.2 Outline 3
2 Cellulose – from fibre to fibril 5
2.1 Nanocelluloses 6
2.1.1 Fibrillated material 8
2.1.2 Crystalline material 9
3 Filtration 11
3.1 Theory of dead-end filtration 12
3.1.1 Average filtration resistance 13
3.1.2 Compressive cakes – the importance of local properties 14
3.1.3 Semi-empirical relations 14
3.1.4 The influence of ionic strength 15
3.2 Theory of electro-assisted filtration 16
3.2.1 Electrophoresis 17
3.2.2 Electroosmosis 17
3.2.3 Ion migration 18
3.2.4 Electrolytic reactions 18
3.2.5 Ohmic heating 18
4 Materials & Methods 19
4.1 Materials 19
4.2 Preparation of the suspensions 19
4.2.1 MCC – the influence of ionic strength 19
4.2.2 Production of TEMPO-MFC 20
4.3 Characterisation 20
4.3.1 Compositional analysis 21
4.3.2 Carboxylate content 21
4.3.3 Zeta potential 22
4.3.4 Focused beam reflectance measurement (FBRM®) 22
4.3.5 Density 22
4.3.6 Surface area 22
4.3.7 Morphology 22
4.4 Filtration Equipment 22
4.4.1 Dead-end filtration 22
4.4.2 Electro-assisted filtration 23
4.5 Experimental conditions 24
4.5.1 Dead-end filtration of MCC 24
4.5.2 Electro-assisted filtration of TEMPO-MFC 24
5 Results & Discussions 25
5.1 Dewatering MCC: The influence of ionic strength 25
5.1.1 Characterisation of MCC 25
5.1.2 Dead-end filtration 27
5.2 Electro-assisted filtration of TEMPO-MFC 29
5.2.1 Characterisation 29
5.2.2 Electro-assisted filtration 30
5.2.3 The dewatering mechanism 32
6 Conclusions & Future Work 35
6.1 Conclusions 35

6.2 Future work..... 36

Nomenclature and abbreviations

A	Area of filter cell [m^2]
c	Mass of solids to volume of filtrate [kg/m^3]
d_γ	Average path length of γ-radiation [m]
K	Permeability [m^2]
n	Model parameter [-]
P_s	Solid pressure [Pa]
P_l	Hydrostatic pressure [Pa]
P_0	Model parameter [Pa]
R_m	Average resistance of filter medium [m^{-1}]
t	Time [s]
v	Superficial velocity [m/s]
v_{solid}	Superficial velocity of the solids [m/s]
V	Volume of filtrate [m^3]
z	Distance from filter medium [m]

Greek letters

α	Local filtration resistance [m/kg]
α_0	Model parameter [m/kg]
α_{av}	Average filtration resistance [m/kg]
β	Model parameter [-]
ε	Porosity [-]
ΔP	Pressure drop across the filter cake and filter medium [Pa]
η_γ	Number of counts [-]
$\eta_{\gamma 0}$	Number of counts in empty filter cell [-]
μ	Dynamic viscosity [Pa s]
$\mu_{\gamma,l}$	Attenuation factor liquid phase [m^{-1}]
$\mu_{\gamma,s}$	Attenuation factor solid phase [m^{-1}]
ρ	Density of liquid phase [kg/m^3]
ρ_s	Density of solid phase [kg/m^3]
φ	Local solidosity [-]
φ_0	Model parameter [-]

Abbreviations

ATR-FTIR	Attenuated total reflectance-Fourier transform infrared spectroscopy
B.E.T.	Brunauer-Emmet-Teller
EDL	Electrolytic double layer
FBRM	Focused beam reflectance measurement
HPAEC-PAD	High performance anion exchange chromatography with pulsed amperometry detection
MCC	Microcrystalline cellulose
MD	Molecular Dynamics
MFC	Microfibrillated cellulose
SEM	Scanning electron microscopy
TEMPO	2,2,6,6-tetramethylpiperidinyl-1-oxyl

1

Introduction

There is a real urgency for industries based on finite resources to adapt to using renewable resources. Valid feed stock that can replace finite resources has to be made available for this shift to be feasible. Cellulose is an example of an outstanding candidate in this context: it is the most abundant biopolymer on Earth and its hierarchical structure allows it to be employed in a multitude of applications. Moreover, the infrastructure is already partly in place in the form of pulp and paper mills.

Cellulose is found in cotton (almost pure cellulose), grass, tunicates, algae and wood; in the latter, it constitutes 40-45% of the wooden matrix (depending on the species). Cellulose-based products have been used for millennia; traditional applications include paper and packaging material, viscose textiles and chemicals (such as carboxymethyl cellulose and hydroxyethyl cellulose). The potential of cellulose does, however, reach further. In recent decades, the intermediate structures of the cellulose fibre, known as nanocelluloses (i.e. fibrillated and nanocrystalline celluloses) have received much attention because of their remarkable mechanical properties, excellent capacity for surface modifications and large surface area. Suggestions have been made, for example, for their use in applications such as nanocomposites, hydrogels, films, barriers and aerogels. A recent Perspective by Li *et al*. [1] covered the potential of fibrillated cellulose, with a very promising outlook. The authors do, however, also acknowledge the challenges that must be overcome in making its production feasible on a larger scale. One such obstacle that must be negotiated is the removal of water from the suspensions.

The removal of water is, nevertheless, an essential operational step in the production of cellulosic materials because the process streams are usually dilute: this is necessary to avoid entanglement and too high a viscosity, for example. At the present, the techniques commonly employed are based on drying, such as spray drying and freeze drying [2]. Unfortunately, these

methods are energy intensive: the addition of a preceding mechanical dewatering step, which usually requires considerably less energy, is a means of reducing the total energy demand.

The most common industrial dewatering technique employed is filtration. This method can, however, be challenging in practice due to the extensive filtration resistance resulting from the large specific surface area. Moreover, if the particle aspect ratio is large, the inherent morphology enables interlocking and interactions between the fibrils, thereby affecting the structure and compressibility of the filter cake. The challenges associated with the dewatering and drying of nanocellulose are summarised further in a review by Sinquefield *et al*. [3] in 2020.

Interparticle interactions are important for filtration, and include electrostatic interactions. Electrostatic interactions are highly influenced by the pH and ionic strength of the cellulose suspension, e.g. agglomeration is promoted when the surface charges of the cellulose particles are shielded efficiently, which affects the total surface area subjected to the liquid flow. Consequently, the structure of the filter cake being formed is influenced. All this, in turn, affects the filtration resistance.

Filtration can also be improved by the use of assisted filtration techniques, whereby additional driving forces are introduced to enhance the filtration rate. One such technique is electro-assisted filtration, where an electric field is introduced across the filtration chamber: this has already been reported to improve the filtration rate of microcrystalline cellulose (MCC) [4,5] and microfibrillated cellulose (MFC) [6]. Applying electro-assisted filtration to MCC has been investigated thoroughly by Wetterling *et al*. [4,5]: it is also worth mentioning their study [7] on the electroosmotic dewatering of cellulose nanocrystals (CNC), in which an electric field alone was used to promote dewatering. Furthermore, only one patent [6] for the application of electro-assisted filtration to MFC has been published thus far. Despite both MCC and MFC being derived from cellulose, their inherent characteristics give rise to different filtration behaviour. MCC has a short rod-like shape and a high degree of crystallinity, whereas MFC has a higher aspect ratio, is flexible and has a great number of hydroxyl groups exposed. Considering these disparities, it thus becomes important to study the electro-assisted filtration of MFC further.

This thesis covers the findings of two papers on the dewatering of cellulose. The first paper investigates the influence of ionic strength during the filtration of MCC and the second is a study of using electro-assisted filtration as a means of improving the dewatering of MFC. The second paper also includes molecular dynamic (MD) simulations with the aim of providing a deeper understanding of the dewatering mechanism at a molecular level, something that has not been reported previously.

1.1 Objectives

The main objective of this work was to explore the filtration of cellulosic materials. It can be divided more specifically into two parts:

- To investigate the influence of ionic strength on dead-end filtration of MCC
- To investigate electro-assisted filtration as a means of improving the dewatering of MFC

1.2 Outline

This thesis summarises the findings of two papers:

1. Dewatering of microcrystalline cellulose: the influence of ionic strength

   An experimental study, in which a suspension of MCC with varying concentrations of NaCl, from 0-1 g/L, was filtered using a dead-end filtration set-up. This set-up allowed for measurements of local solidosity and hydrostatic pressure to be made.

2. Electro-assisted filtration of microfibrillated cellulose: insights gained from experimental and simulation studies

   A combined experimental and simulation study. In the experimental work, a suspension of MFC produced via 2,2,6,6-tetramethylpiperidinyl-1-oxyl (TEMPO)-mediated oxidation was dewatered using a modified version of the dead-end filtration set-up, in which an electric field was applied across the lower part of the filter cell. MD simulations were performed to gain further insights into the dewatering mechanism on a molecular scale.

The first two chapters to follow cover the theoretical background of cellulose and filtration, respectively. The fourth chapter presents the materials and methods, whilst the results and discussion follow in the fifth. The sixth, and final, chapter is the conclusions that are drawn and suggestions for future work.

2

Cellulose - from fibre to fibril

"*Cellulose is the most abundant polymer in nature…*"

A large quantity of cellulose is derived from forests: depending on biological origin, cellulose constitutes around 40-45 % of wood [8]. The majority of the remaining wooden matrix is comprised of hemicelluloses and lignin. Wood presents a hierarchical structure (Fig. 2.1a), spanning from the trunk (m) down to the monomeric structures (Å). It is therefore important that this hierarchical structure is studied in order to understand how cellulose, at its different length scales, can be liberated and utilised.

The cellulose chain is formed of linear D-anhydroglucopyranose units linked together by β-(1→4)-glucosidic bonds. Three hydroxyl groups are located on C2, C3 and C6 on each anhydroglucose unit, see Fig. 2.1b. It is the strong intra and inter hydrogen bonding between the hydroxyl groups at the different anhydroglucose units that makes the cellulose chains form sheets and provides cellulose with its stiff character.

The cellulose chains, which are extruded from cellulose-synthesizing hexametric complexes in the plasma membrane, are stacked up as parallel sheets interacting through attractive van der Waals forces and hydrophobic interactions to form elementary fibrils [9] with a diameter of 3-4 nm [10]. Not all details of this process are known, and it is the subject of debate whether 18, 24 or 36 cellulose chains constitute the elementary fibril [11]. Another widely debated topic is the development of the "twist" in the elementary fibril [12] that causes it to have both ordered and disordered regions, where the latter are more prone to reactions.

Elementary fibrils are aggregated into so-called microfibrils[1] which, in turn, can aggregate to form macrofibrils by interacting via van der Waals forces and hydrogen bonding.

Cellulose microfibrils are found in the wood cell, which is comprised of several layers: the middle lamella (M), the primary wall (P) and the secondary layer that consists of three layers (S1, S2 and S3). The middle lamella is rich in lignin and provides contact with the neighbouring cell, whereas the other layers contain varying amounts of cellulose, hemicellulose and lignin in a complex matrix. Cellulose microfibrils are found in a random pattern in the primary layer, whereas they are located at alternating angles in the secondary layer: the microfibril angle (MFA) is important for the flexibility of the cell wall [13].

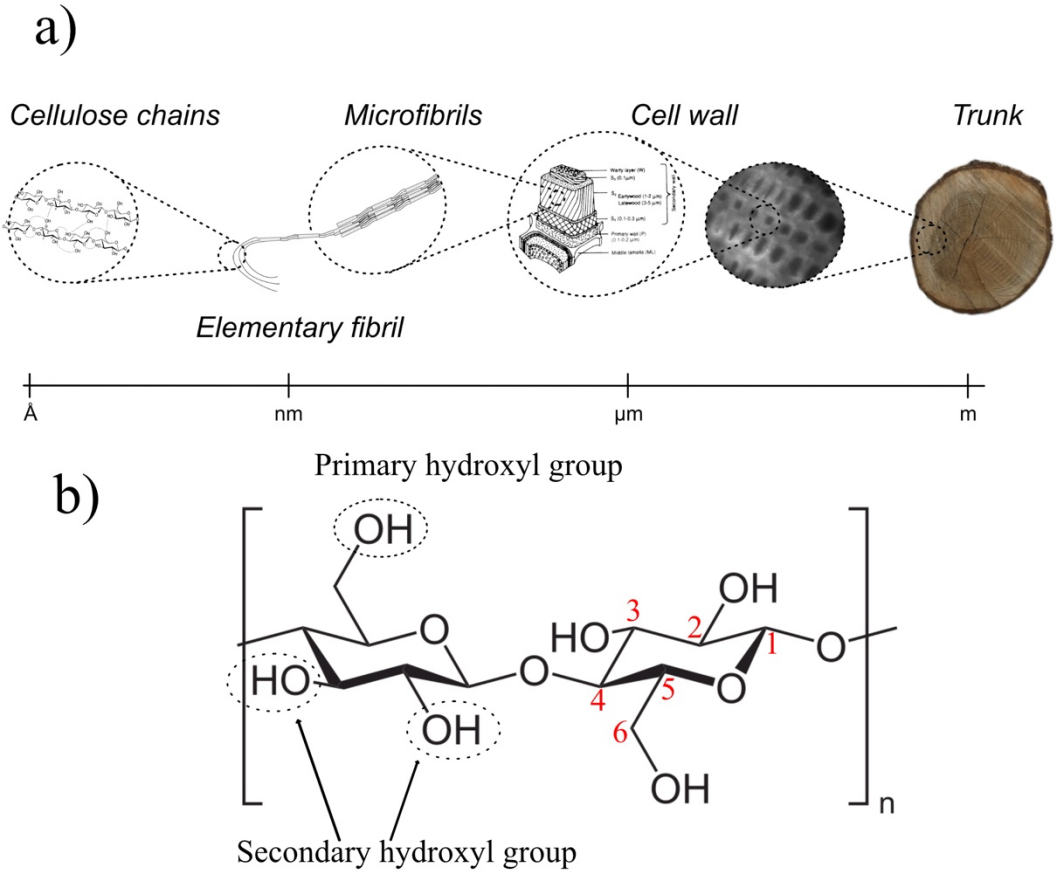

Figure 2.1 Overview of cellulose. a) Schematic diagram of the hierarchical structure. Cell wall model adapted from Huang *et al*. [14]. b) Cellobiose unit, with hydroxyl groups encircled with dashed lines and the number of the carbon atom given in red.

2.1 Nanocelluloses

Materials isolated from cellulose, with at least one dimension in nanoscale, are referred to as nanocelluloses. This has been a hot research topic during the past 15 years or so, with a steadily increasing number of publications as shown in Fig. 2.2. One reason behind this is associated with the efforts being made to maximize the potential of sustainable raw materials such as cellulose. Expanding knowledge of nanocelluloses makes it increasingly possible to use all structures of cellulose efficiently and thereby ensure that none of these structures are neglected. Nanocelluloses have been found to possess unique properties, such as a low density (around

[1] Although the terminology is under debate among scholars, some refer to microfibrils as elementary fibrils whilst others claim that microfibrils consist of several elementary fibrils.

1.6 g cm^{-3}), high aspect ratios, good mechanical properties, optical properties and a favourable capacity for surface modifications. The different cellulose materials can, in turn, be used in a variety of products with variable properties: mechanical, thermal, optical and rheological.

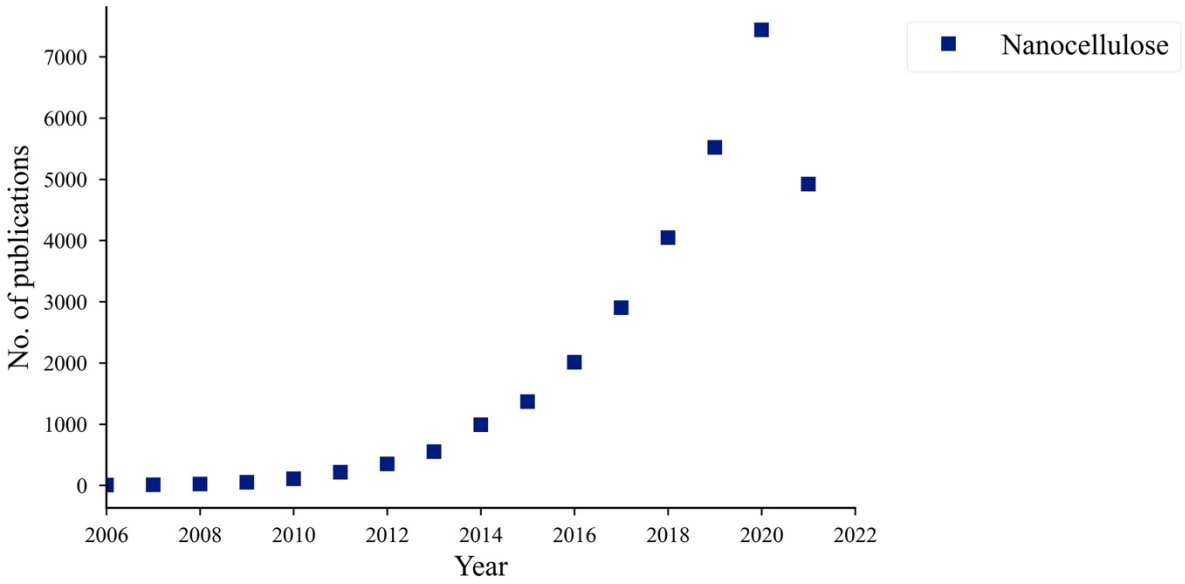

Figure 2.2 Number of publications pertaining to "Nanocellulose" according to Scopus [2021-06-17, Search word= "Nanocellulose"]. NB: The figure for 2021 is ongoing.

Nanocelluloses derived from wood include micro/nanofibrillated cellulose and nanocrystalline cellulose, see Fig 2.3. The nomenclature for these materials is rather scattered within the research field, with microfibrillated cellulose being referred to as MFC, nanofibrillated cellulose as CNF or NFC and cellulose nanocrystals as CNC or NCC. Although the former terms refer to fibrillated material, it is difficult to distinguish between the two terms [15]. Many scholars claim the distinction is related to the degree of fibrillation: NFC is fibrillated into elementary fibrils, whereas MFC is not as heavily fibrillated [16]. The present work employs this same distinction between fibrillated materials, and the abbreviations used are therefore MFC, NFC and CNC.

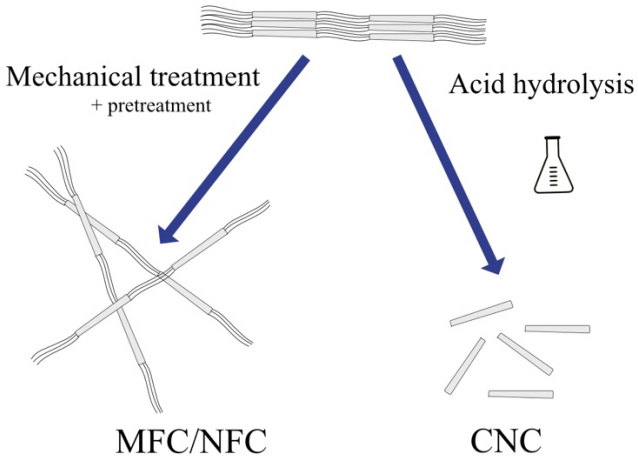

Figure 2.3 Simplified flow chart illustrating the two methods used for producing MFC/NFC and CNC.

2.1.1 Fibrillated material

Microfibrils and elementary fibrils may be isolated from the cellulose fibre to obtain MFC and NFC. The liberation of the cellulose fibrils is achieved by mechanical methods, e.g. high-pressure homogenisers, microfluidizers and cryo-crushing. Such mechanical liberation is energy intensive and various pre-treatments are therefore used as a means of reducing the energy demand: chemical [17–19] and/or enzymatical [20].

Fibrillated materials are flexible and have a large aspect ratio with a large number of hydroxyl groups exposed. These characteristics contribute to an excellent mechanical strength (tensile strength of 4.9-7.5 GPa is reported [1]): the hydroxyl groups enable formation of intra- and intermolecular hydrogen bonds and the fibrils may entangle thereby toughening the material. However, the entanglement of the fibrils may also be disadvantageous as it may cause clogging during the mechanical disintegration in the high-pressure homogeniser.

The tale of MFC began in the 1980s following the discoveries made by Turbak *et al*. [21] and Herrick *et al*. [22]. They used high-pressure homogenisers to liberate the cellulose fibrils, thereby obtaining the first samples of MFC. However, the energy demand of the liberation process was extensive, and the process suffered from severe clogging issues [23]. Despite continued research on the new fibrillated material during the late 1980s, e.g. by Wågberg *et al*. [24] and Lindström and Winter [25], interest from industry was lacking.

New approaches that were taken to make the liberation process more energy efficient nonetheless revived interest in MFC in the beginning of the 21th century; in particular the work by Saito and Isogai [19]. They introduced repelling forces through conversion of the primary hydroxyls on the cellulose surface into carboxylate groups, via TEMPO-mediated oxidation, as a means of facilitating the separation of fibrils.

Figure 2.4 presents the reaction scheme of the TEMPO-mediated oxidation of cellulose using a TEMPO/NaBr/NaClO reactant mixture, where TEMPO has the role of the catalyst, bromide is the co-catalyst and sodium hypochlorite is the primary oxidant. TEMPO, in its radical form, is highly reactive and easily oxidised to a nitrosonium cation by the primary oxidant. The nitrosonium ion reacts with the primary alcohol on the cellulose surfaces and converts them into aldehydes, which are oxidised further into carboxylate groups. The kinetics are highly dependent on the pH: an alkaline pH of around 10-11 has been reported as being optimal for converting the primary hydroxyl group [10]. Sodium hydroxide must be added to maintain the desired pH, since hydrogen ions are formed during the reaction.

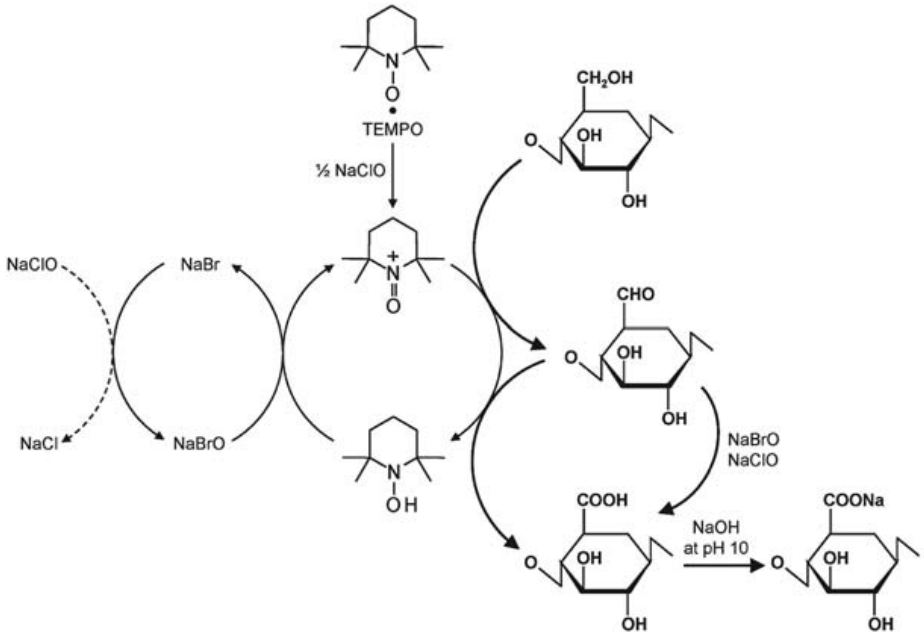

Figure 2.4 Reaction scheme of TEMPO-mediated oxidation. Reproduced from Isogai *et al.* [26] with permission from the Royal Society of Chemistry.

2.1.2 Crystalline material

CNCs, in contrast to fibrillated cellulose, are produced by breaking the glucosidic bonds between the less ordered parts of the cellulose microfibrils, thereby resulting in stiff rod-like fractions. Such disintegration is achieved through hydrolysis with a mineral acid, which is usually sulphuric acid although other acids can also be used. Following acid hydrolysis, the suspension is diluted, and any remaining impurities are removed through centrifugation and dialysis. Finally, the cellulose nanocrystals are dispersed into a stable suspension via sonication [23].

It should also be mentioned that a milder acid hydrolysis of cellulose-rich material results in the production of MCC in which some amorphous parts remain. After hydrolysis, the material is neutralized and dried, commonly via a spray drying technique [27]. Avicel® is a well-known example of MCC and is used in a variety of products ranging from toothpaste and pharmaceuticals to cosmetics.

3

Filtration

"Reaction engineering tells whether the process is possible or not:
the separation whether the process is profitable or not."

-Prof. Ann-Sofi Jönsson
(Avancell 2019)

Filtration is a mechanical separation technique, commonly applied in solid-liquid separation. It is used in a wide range of applications, from brewing coffee to dewatering sludge and concentrating product streams. The filtration operation can, if needed, be followed by thermal drying to further increase the dry content of the solid material. The cost of mechanical dewatering is usually lower than that of thermal dewatering, so it is of the essence that the former unit operation is as efficient as possible.

Conventional filtration (i.e. pressure driven) is, however, not always the most suitable option. This is true, for instance, when handling suspensions in which particles of high specific surface area are subjected to flow: in these cases, assisted filtration techniques are suggested. One such technique is electro-assisted filtration, where an electric field is applied across the filtration chamber. The application of an electric field introduces additional driving forces, such as the electroosmotic flow of water and the electrophoretic movement of particles, which promote dewatering and thereby modify the structure of the filter cake being formed.

3.1 Theory of dead-end filtration

Dead-end filtration, also known as cake filtration, is a filtration method alongside depth filtration and crossflow filtration. In dead-end filtration, the separating agent (i.e. the filter medium) allows the liquid in a suspension to pass through but not the particles as a result of the pressure difference between the side of the filtrate and that of the suspension: this is the driving force. Consequently, a filter cake is built up as the liquid is removed from the suspension.

The flowing liquid acts on the particles in the filter cake formed through skin friction, thereby causing drag forces to be exerted. These stresses are accumulated via point connections through the filter cake towards the filter medium, and is referred to as solid pressure, $P_s(x,t)$. The hydrostatic pressure therefore decreases during filtration at a given position in the filter cake as it grows.

A local force balance across a thin section of the filter cake gives the following relationship between the hydrostatic and solid pressures:

$$-dP_l = dP_s \tag{3.1}$$

Given Eq. 3.1, the following can be used if gravitational forces are neglected:

$$P_{cake}(t) = P_l(x,t) + P_s(x,t) \tag{3.2}$$

where *l* and *s* refer to the hydrostatic and solid pressure, respectively. In Eq. 3.2, it is important to note that whilst P_{cake} varies with time, the hydrostatic and solid pressures vary with time and position [28]. However, in the case of constant applied pressure and negligible pressure drop across the filter medium, the latter is independent of time.

The flow of liquid through the filter cake can be seen as flow through a porous medium. Many important discoveries on flow through porous medium were realised during the 19th century by Darcy in his work on the fountains of Dijon [29]. Although Darcy himself did not include viscosity in the original expression, the equation presented in Eq. 3.3 is often referred to as Darcy's law. The differential form of Darcy's law is expressed as:

$$v = -\frac{K}{\mu}\frac{dP_l}{dz} \tag{3.3}$$

where v is the superficial flow velocity, K is the permeability of the bed, μ is the dynamic viscosity and dP_l/dz is the hydrostatic pressure gradient.

The relation between the permeability of the bed and the average filtration resistance is defined according to Eq. 3.4 thus:

$$K = \frac{1}{\alpha \rho_s \varphi} \tag{3.4}$$

where α is the specific filtration resistance, ρ_s is the solid density and φ is the solidosity, which is the volume of solids in relation to the total volume.

If Eq. 3.4 is combined with Eq. 3.3, the expression of the velocity is altered and the resulting expression is as presented in Eq. 3.5:

$$v = -\frac{1}{\mu\alpha\rho_s\varphi}\frac{dP_l}{dz} \quad (3.5)$$

It is actually rather inconvenient to include the height of the filter cake, as this may be difficult to measure in industrial filters, and it is therefore more common to use the surface weight of the cake, *w*, expressed as kg solid material/m^2. The expression of the surface weight of a thin slice of the filter cake is expressed in Eq. 3.6 as:

$$dw = \varphi\rho_s dz \quad (3.6)$$

Combining Eqs. 3.5 and 3.6 gives, after a little rearrangement, Eq. 3.7:

$$-\frac{dP_l}{\alpha} = v\mu dw \quad (3.7)$$

3.1.1 Average filtration resistance

An important parameter in dead-end filtration is the average filtration resistance, which can be calculated from the equation once proposed by Ruth *et al*. [30]. He used an analogy to electrical resistances in series to describe the flow through a filter cake and a filter medium, respectively. The total pressure drop, ΔP, expressed according to Eq. 3.8, is equal to the pressure drop across the filter cake, P_{cake}, and over the filter medium, P_{medium} (Eq. 3.9). The pressure drop across the filter cake is obtained by integrating Eq. 3.7 across the filter cake and is expressed in Eq. 3.10 thus:

$$\Delta P = P_{cake} + P_{medium} \quad (3.8)$$

$$P_{medium} = v\mu R_m \quad (3.9)$$

$$P_{cake} = v\mu\alpha_{av}w_{cake} \quad (3.10)$$

where α_{av} is the average specific filtration resistance and R_m is the resistance of the filter medium.

Finally, the differential form of the classical filtration equation [30] (Eq. 3.11) is obtained by replacing w_{cake} with cV/A and expressing the velocity as: $v = \frac{1}{A}\frac{dV}{dt}$

$$\frac{dt}{dV} = \frac{\mu c\alpha_{av}}{A^2\Delta P}V + \frac{\mu R_m}{A\Delta P} \quad (3.11)$$

where *c* is the mass of solids per unit of filtrate volume, *A* is the area of the filter cell and *V* is the filtrate volume obtained at time t.

Plotting dt/dV versus V yields a linear plot, given constant applied pressure, from which α_{av} can be calculated from the slope of the line and R_m from its intercept. The integrated form of Eq. 3.11 can also be used, but the differential form is preferred as it uses instant values.

The classical filtration equation presented in Eq. 3.11 is developed using the following assumptions, thereby restricting its use to incompressible filter cakes or filter cakes with limited compressibility:

- The velocity of the solid is zero
- The solidosity is constant throughout the cake
- No blinding effects of the filter medium occur
- The filtrate is only liquid, i.e. all particles are retained on the membrane side

3.1.2 Compressive cakes – the importance of local properties

In reality, however, the structure of most filter cakes (and thus its properties) varies throughout, so the cake is not incompressible: the solid structure will, instead, collapse as a consequence of the solid pressure increasing in the direction towards the membrane. The cake is therefore regarded as being compressible, which means that its properties vary across the structure, e.g. the velocity of flowing liquid increases as the pores become reduced in size towards the membrane.

The compressible structure of filter cakes makes it important to study their local properties, such as local solidosity, local hydrostatic pressure and local filtration resistance.

3.1.2.1 Solidosity

Solidosity, φ, is defined as the volume of solids in relation to the total volume and is related to porosity, ε, according to Equation 3.12.

$$\varphi = 1 - \varepsilon \tag{3.12}$$

The solidosity of a filter cake can be determined by several methods: cake dissection [31], nuclear magnetic resonance [32], conductivity measurements [33] and γ-ray attenuation [34]. The latter is a non-invasive method that allows the solidosity to be calculated using Beer-Lambert's law for two phases, as given in Eq. 3.13.

$$-ln\frac{\eta_\gamma}{\eta_{\gamma 0}} = \mu_{\gamma,l} d_\gamma + (\mu_{\gamma,s} - \mu_{\gamma,l})\varphi \tag{3.13}$$

where η_γ is the number of counts recorded per time, $\eta_{\gamma 0}$ is the number of counts for the empty filter cell, μ_γ is the attenuation factor (l and s equal liquid and solid, respectively), d_γ is the average path length of the radiation and φ is the solidosity.

3.1.2.2 Local filtration resistance

In the case of compressible cakes, the modified Darcy's equation developed by Shirato *et al.* [35], and presented in Eq. 3.14, may be used to express the flow through the filter cake in one dimension when the solid particles are not considered to be stationary. Combining Eqs. 3.14 and 3.4 allows the local filtration resistance to be determined.

$$v - \frac{1-\varphi}{\varphi} v_{solid} = -\frac{K}{\mu}\frac{dP_l}{dz} \tag{3.14}$$

In practice, however, the velocity of particles is considered as being much less than that of the flowing liquid and thus v_{solid} is approximated as zero.

3.1.3 Semi-empirical relations

There are several models for evaluating the compressibility of a filter cake, although they usually lack physical bearing and are merely empirical. Tiller and Leu [36] suggested the use of semi-empirical relations when studying the relation between the solid pressure (Eq. 3.15) and the solidosity and local filtration resistance (Eq. 3.16).

$$\varphi_i = \varphi_0 \left(1 + \frac{P_s}{P_0}\right)^{\beta} \quad (3.15)$$

$$\alpha_i = \alpha_0 \left(1 + \frac{P_s}{P_0}\right)^{n} \quad (3.16)$$

φ_0 and α_0 may be interpreted as the solidosity and local filtration resistance at zero compressible pressure, respectively. P_0, β and n are mere empirical parameters, where the two latter are related to the compressibility of the specific material. The five parameters may be determined by simultaneous fitting of local experimental data.

The parameters in the semi-empirical relations mentioned above may be used to evaluate the degree of compressibility. In his doctoral thesis, Leu [37] suggested a categorisation of n, β and φ_0 as reported in Table 3.1.

Table 3.1 Categorization of the model parameters in Eqs. 3.15 and 3.16 according to Leu [37]

	Low compressibility	Medium compressibility	High compressibility
α_0 [m/kg]	10^9	10^{10}	10^{11}
φ_0 [-]	0.30	0.20	0.10
β [-]	0.05	0.15	0.30
n [-]	0.20	0.60	1.20

The average filtration resistance can be calculated from the semi-empirical correlations. The definition of the average filtration resistance, shown in Eq. 3.17, should be revisited in order to achieve the expression being sought.

$$\frac{1}{\alpha_{av}} \equiv \frac{1}{P_{cake}} \int_0^{P_{cake}} \frac{dP_s}{\alpha} \quad (3.17)$$

Finally, the average filtration resistance (Eq. 3.18) can be calculated using local filtration data by combining Eq. 3.16 with the definition of the average filtration resistance, i.e. Eq. 3.17 thus:

$$\alpha_{av} = \alpha_0 \frac{(1-n)\frac{P_{cake}}{P_0}}{\left[\left(1+\frac{P_{cake}}{P_0}\right)^{1-n} - 1\right]} \quad (3.18)$$

3.1.4 The influence of ionic strength

The interparticle interactions that occur during filtration can be altered, which may influence the filtration process: these include repulsive electrostatic interactions, attractive van der Waals forces, friction and interlocking of particles. The focus in this thesis is on the former, i.e. the influence of electrostatic interactions.

Electrostatic interactions can be changed by, for example, adjusting the pH of the suspension, as in a study on the dead-end filtration of MCC carried out by Mattsson *et al*. [38]. They concluded that lowering the pH caused protonation of the carboxylic acid groups originating from the chemical isolation process [39], which reduced the magnitude of the electrostatic interactions between the MCC particles and thus promoted agglomeration. This, in turn, resulted in a decreased filtration resistance, since the surface area of the MCC subjected to the liquid flow decreased.

Another way of altering electrostatic interactions is to vary the ionic strength of the solution. The consequence of adding ions requires the electrolytical double layer (EDL) theory to be explained. The EDL theory is well known: a particle in a polar medium is attributed with a surface charge due to mechanisms that include ionisation and adsorption. A particle that carries a surface charge will be surrounded by a double layer of counterions, referred to as EDL. Figure 3.1 shows the EDL model and is comprised of two layers: stern and diffusive. The former represents a compact region of immobile counterions closest to the charged surface of the particle whereas the latter contains mobile ions, with varying charge densities from the surface.

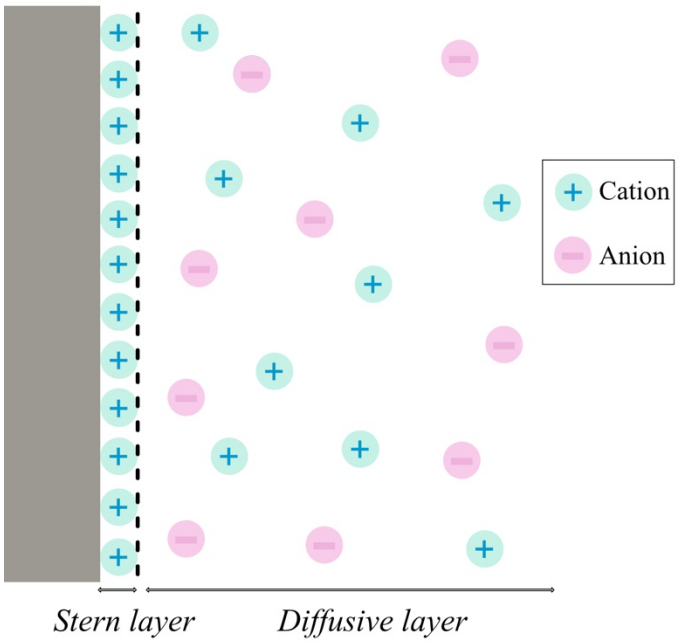

Figure 3.1 The EDL theory shown schematically. Grey rectangle: a particle with negative surface charge.

The diffuse layer needs to be smaller in volume upon the addition of counterions because its concentration of counterions increases, and the EDL is then said to be compressed. Consequently, the repulsive electrostatic forces between the particles become less dominant at a certain distance from the particle surface and the surface charges are shielded more efficiently. If the reduction of the electrostatic interactions is sufficiently large, the attractive van der Waals forces become predominant, and the particles start to agglomerate. When this happens, the specific surface area subjected to the liquid flow will be altered and thereby affect the filtration.

The effect that ionic strength has on filtration has been studied in a number of publications [40–45]. Although different materials have been investigated, an increase in the rate of dewatering upon the addition of ions has been reported in several publications. For example, Sim *et al*. [44] reported that the dewatering of a suspension of nanofibrillated cellulose increased with increasing concentration of NaCl, and Ruth *et al*. [45] made similar observations when adding 0.5 M NaCl to a Filter-Cel suspension.

3.2 Theory of electro-assisted filtration

Electro-assisted filtration has been used to improve the dewatering of various hard-to-dewater materials such as sludge [46,47], clay [48,49] and biopolymers [50,51] by introducing additional driving forces through the application of an electric field. Several electrokinetic phenomena occur when an electric field is applied across the filter chamber, some of which are beneficial for dewatering whilst others are not. These phenomena include electrophoresis,

electroosmosis, ion migration, ohmic heating and electrolysis [52], the first three of which are explained further for the dead-end filtration set-up shown in Fig. 3.2.

The phenomena are explained for a particle carrying a negative surface charge, as this is what cellulose particles carry at standard conditions due to deprotonation of the acidic groups originating from the pulping process [39]. In addition, surface modifications that are used to aid mechanical disintegration commonly introduce negative surface charges on the surface of the cellulose.

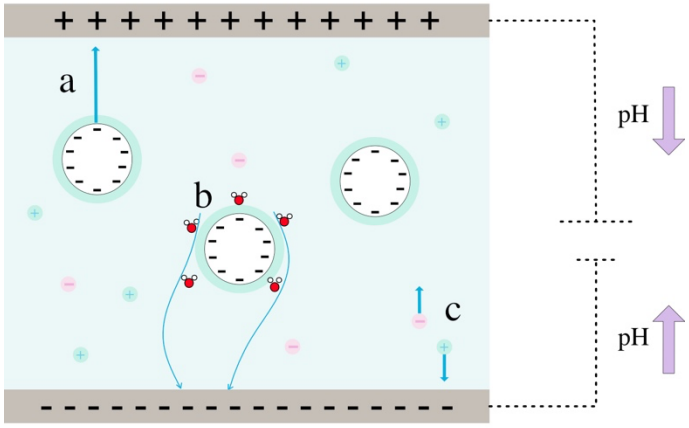

Figure 3.2. Schematic diagram of the electrokinetic phenomena that occur when an electrical field is applied in a suspension with particles carrying a negative surface charge (white circles). Turquoise dots: cations. Pink dots: anions. a) electrophoretic movement, b.) electroosmotic flow, c.) ion migration.

3.2.1 Electrophoresis

Electrophoresis, presented in Fig. 3.2a, is defined as the relative movement of negatively charged particles in a solution towards the anode. When the cathode is placed beneath the filter medium, the electrophoretic movement may counteract the build-up of a filter cake if it surpasses the drag force on the particle: this reduces the filtration resistance, and can hence be considered as being beneficial to dewatering [53]. The electrophoretic movement continues until the particle encounters a hindrance, for example by being restricted by a filter cake or encountering an electrode.

3.2.2 Electroosmosis

Upon the application of an electric field, the layer of cations surrounding the negatively charged particles (see Ch. 3.1.4 The influence of ionic strength) is transported towards the cathode along with the bulk water: this is known as electroosmosis and is presented in Fig. 3.2b. The Helmholtz-Smoluchowski Equation (Eq. 3.19) is often used to express the electroosmotic flow of a liquid [54]:

$$\frac{\upsilon}{E} = \frac{\varepsilon\varepsilon_0\zeta}{\eta} \qquad (3.19)$$

where υ is the electroosmotic velocity, E is the strength of the applied electric field, ε is the relative dielectric constant of the fluid, ε_0 is the permittivity of vacuum, ζ is the zeta potential and η is the dynamic viscosity of the dispersion medium.

3.2.3 Ion migration

Ion migration is the transport of ions towards the oppositely charged electrode, see Fig 3.2c. Ionic products formed in the electrolysis reactions (see Ch. 3.2.4 Electrolytic reactions) may migrate to the filter cake through ion migration [55].

3.2.4 Electrolytic reactions

Electrolysis reactions, in which water is decomposed, take place at the respective electrode, thus [56]:

Anode: $2H_2O\ (l) \rightarrow 4H^+ + O_2\ (g) + 4e^-$

$M^{n+} + ne^- \rightarrow M$

Cathode: $2H_2O\ (l) + 2e^- \rightarrow 2OH^- + H_2\ (g)$

$M \rightarrow M^{n+} + ne^-$

where M is the material of the electrode and M^{n+} its cation.

The decomposition of water results in the formation of a pH gradient between the electrodes, as hydrogen ions are formed at the anode and hydroxide ions at the cathode. This causes a reduction in the pH at the anode side and an increase in the pH at the cathode side, as indicated in Fig. 3.2. A change in pH may influence the dewatering process as it could alter the zeta potential of the particles in the suspension, thereby affecting the electrokinetic phenomena [57] or promoting particle aggregation [58]. In addition, a non-conducting gas may be created via electrolysis reactions at the electrodes, potentially causing an electrical resistance [59].

3.2.5 Ohmic heating

The passage of a current through the system causes ohmic heating (Eq. 3.20) thus:

$$Q = I^2R \qquad (3.20)$$

where Q is ohmic heating, I is the current (A) and R is the electrical resistance of the system (ohm).

The temperature between the electrodes increases as a consequence; this, in turn, decreases the viscosity of the liquid and filtration is thereby aided. Overheating can, however, lead to the destruction of e.g. the electrodes and filter medium and thus have a negative effect [60].

4

Materials & Methods

This chapter will describe the materials and methods used in the two papers included.

4.1 Materials

Microcrystalline cellulose (Avicel® PH-105) supplied by DuPont Nutrition was the model material used. According to the manufacturer, it had an average nominal particle size of 19 µm, which was determined by a method based on laser diffraction. The concentration of NaCl in the suspension was adjusted using 2 M NaCl (VWR GPR Rectapur).

MFC was produced by the TEMPO-oxidation of a dissolving pulp sourced from a Scandinavian pulp mill. The material is referred hereafter as TEMPO-MFC. The chemicals used were NaClO (10-15% available chlorine) from VWR, TEMPO (98%) and NaBr (>99.5%), both from Sigma Aldrich. In addition, NaOH (Sigma Aldrich) was used to regulate the pH during oxidation.

4.2 Preparation of the suspensions

4.2.1 MCC – the influence of ionic strength

A sample of MCC was suspended in 2 L of deionized water to a concentration of 10% by volume before being treated mechanically with an IKA Ultra-Turrax® T50 with a dispersing element (S50 N-G45F). It was then diluted further to a concentration of 5% by volume and stirred continuously overnight. The ionic strength of the suspension was varied by adding a calculated amount of 2 M NaCl to 1 L of MCC suspension under simultaneous stirring 1 h prior to the filtration experiment. The ionic concentrations used were 0.0, 0.10, 0.15, 0.20, 0.50 and 1.0 g/L NaCl, respectively.

4.2.2 Production of TEMPO-MFC

NaBr (1 mmol/g pulp) and catalytic amounts of TEMPO (0.1 mmol/g pulp) were added to a suspension containing 40 g (dry basis) of dissolving pulp and deionised water in a baffled vessel under constant stirring with a four-pitch blade impeller. The reaction was initialised by the dropwise addition of NaClO, carried out at a pulp concentration of 1 wt.% and at ambient temperature. A pH of 10.1 ± 0.1 was maintained throughout the reaction by the addition of 0.5 M NaOH; it was quenched using 200 ml 99 % EtOH after 70 minutes had lapsed.

The oxidised fibres were separated by vacuum filtration. Smaller fibre fragments were retained by recirculation of the first volume of filtrate. The oxidised fibres were washed repeatedly with deionised water and the resulting conductivity of the filtrate was <20 µS/cm. The oxidised pulp was stored in plastic bags at 4 ºC until required for further treatment and analysis.

TEMPO-MFC was produced by treating a 1 wt.% suspension of the oxidised pulp mechanically, using an IKA Ultra-Turrax® T50 with a dispersing element (S50 N-G45F) operating at 10 000 rpm for 4 min/g TEMPO-oxidised pulp. A solids content of 1 wt.% was used to limit the viscosity.

4.3 Characterisation

Thorough characterisation of the cellulose material is important because of the inherent differences of the raw material and the methods used for their production. The characterisation methods employed in the two papers are summarized in Table 4.1 below.

Table 4.1 Summary of the different characterisation methods employed on the cellulose material in the two papers.

MCC	**Dissolving pulp**	**TEMPO-oxidised pulp**	**TEMPO-MFC**
Compositional analysis	Compositional analysis		
	Conductometric titration		Conductometric titration
	ATR-FTIR	ATR-FTIR	
Zeta potential			Zeta potential
Focused Beam Reflectance Measurement (FBRM)			
Density			
B.E.T. surface area			B.E.T. surface area
SEM (Morphology)			SEM (Morphology)

4.3.1 Compositional analysis

A method based on the work of Theander and Westerlund [60] was utilised to determine the composition of the raw materials in terms of monosugars and lignin. In brief, the raw material is disintegrated into a solution of monosugars and acid soluble lignin (ASL) through acid hydrolysis with sulphuric acid. Not all the lignin is solubilised in this process: some remains in the form of a precipitate, and is referred to as Klason lignin (KL).

The monosugars were quantified using a high performance anion exchange chromatography with pulsed amperometry detection (HPAEC-PAD) system (Dionex ICS-5000 equipped with CarboPac PA1 columns), with fucose as an internal standard. The eluents used were NaOH/NaAc (aq.) and NaOH (aq.). The ASL was quantified by measuring the absorbance with UV at 205 nm (Specord 205, AnalytikJena) using an absorptivity constant of 110 $dm^3g^{-1}cm^{-1}$, whereas the amount of KL was determined gravimetrically.

4.3.2 Carboxylate content

Qualitative and quantitative measurements of the carboxylate content were performed by ATR-FTIR and conductometric titration, respectively.

The sample of pulp, which had been dried at 60 ºC for at least 24 h to remove any moisture, was placed on top of an Attenuated Total Reflectance (ATR) crystal and clamped in place to ensure that an even pressure was applied. The infrared spectrum was recorded in transmittance mode, with a resolution of 4 cm^{-1} recording from a wavenumber of 400 to 5000 cm^{-1}, using a PerkinElmer Frontier.

The method of conductometric titration employed for the TEMPO-MFC is based on the work by Mautner *et al*. [61]. A sample of 0.15 g (dry weight) TEMPO-MFC was diluted to 60 ml with deionised water and 5 ml of 10 mM NaCl solution. It was then left to stabilise before the pH was adjusted to 2.5-3 using 0.1 M HCl. Titration with 40 mM NaOH at a dosing rate of 0.1 ml/min was carried out, with subsequent monitoring of the conductivity performed using a digital conductivity meter (model CO 301, VWR). Nitrogen was bubbled through the system throughout the titration process to limit the influence of CO_2. The carboxylate was calculated according to Eq. 4.1 thus:

$$n = \frac{(v_1 - v_0)c_{NaOH}}{m} \qquad (4.1)$$

where n is the carboxylate content (mmol/g TEMPO-MFC), v_1 and v_0 are the volumes of NaOH (mL) at the intersection points between the plateau and the linear regions and is determined graphically, c_{NaOH} is the concentration of NaOH (mmol/mL) and m is the mass of TEMPO-MFC (g). Titration was performed in duplicate.

The carboxylate content of the unoxidised pulp was determined using the SCAN-CM 65:02 protocol. Approximately 1 g of pulp (dry basis) was washed with 0.01 M HCl until a conductivity of below 5 µS/cm was obtained. 5 ml of 0.1 M HCl and 10 ml 0.01 M NaCl was added to the washed fibres in a total volume of 500 ml. The suspension was then titrated with 0.05 M NaOH. The carboxylate content was calculated from Eq. 4.1, in which m is changed to equal the mass of pulp, so n equals mmol/g pulp.

4.3.3 Zeta potential

The zeta potential of 5 vol.% MCC suspensions with a concentration of 0.06-1 g/L NaCl was measured using DelsaMax PRO (Beckman Coulter). Furthermore, the zeta potential of the polyethersulphonate (PES) membrane was measured using an Anton Paar SurPASS streaming potential analyser for planar geometry.

The zeta potential of the TEMPO-MFC was measured using a Zetasizer Nano ZS (Malvern Instruments); a 0.05 wt.% solution with a background concentration adjusted to 5 mM NaCl was used to ensure a finite double layer thickness around the fibrils [62].

4.3.4 Focused beam reflectance measurement (FBRM®)

The way in which the agglomerate/particle size of the MCC varied under the influence of increasing concentration of NaCl was studied using FBRM® (Mettler Toledo). This involves passing a focused beam of laser light through a sapphire window located at the end of the FBRM probe. The laser light scans in a circular path and, when it scans across a particle, the back-scattered light is directed back to the probe. Using the time required for the laser beam to cross through the particle, along with the scanning rate of the laser beam, allows the particle/agglomerate chord length (reported as #/s in the iC FBRM software) to be calculated which, in turn, can be related to the particle size.

4.3.5 Density

The solid density of the MCC was ascertained by a gas pycnometer (AccuPyc II 1345, Micromeritics®), using helium as the displacement gas. This method is non-destructive: the solid density of the material is determined from knowledge of the mass of the sample and its volume, which is obtained through a method based on gas displacement.

4.3.6 Surface area

Nitrogen adsorption at 77 K, using the Brunauer–Emmett–Teller (B.E.T.) method, was used to evaluate the specific surface area. MCC and TEMPO-MFC were both subjected to a solvent exchange procedure in order to preserve the water-swollen state. In the method used, adapted from Wang *et al*. [63], water is first replaced by acetone and followed by displacement washing. This is repeated 5 times, whereafter the same procedure is repeated with cyclohexane. The material is then dried in a nitrogen atmosphere overnight.

4.3.7 Morphology

Scanning Electron Microscopy (SEM) using FEI Quanta200 ESEM was used to investigate the morphology of the MCC (after undergoing the aforementioned solvent-exchange, see Ch. 4.3.5 Surface area) and the TEMPO-MFC (a droplet of 0.005 wt.% TEMPO-MFC was allowed to air-dry overnight on top of a polished SEM stub). A low voltage was used (3 kV) to prevent the samples from burning.

4.4 Filtration Equipment

4.4.1 Dead-end filtration

The filtration set-up was a pneumatically-driven piston press (Fig. 4.1) capable of handling pressures up to 60 bar.

The filter cell has an inner diameter of 0.06 m and a total height of 0.175 m; the lower part, which is made of Plexiglas (h=0.115 m), is placed upon a perforated bottom plate. The pressure capillaries are mounted through the bottom plate and have circular holes of 0.6 mm located

perpendicular to the flow at a distance from the bottom plate of 0.5, 1, 2, 3, 5, 7, 9 and 12 mm, respectively. The pressure capillaries have conical tops to minimise disturbance to the flow. Prior to the filtration experiments, the capillaries are flushed thoroughly with degassed water to remove air, which would cause entrapment of the suspension and thereby provide inaccurate measurements. The pressure capillaries are connected to pressure transducers (Kristal Instrument AG, accuracy of 10 kPa) and the absolute hydrostatic pressure is recorded in LabVIEW™ (Software Version 15.0, National Instruments) every other second. LabVIEW is also used to record the position of the piston and the mass of the filtrate using a balance (Mettler Toledo SB 32000) with an accuracy of 0.5 g.

A γ-emitting ^{241}Am source of 10^9 Bq was the origin of the radiation used for the solidosity measurements. The attenuation of the γ-radiation in a 1 mm thick slice of filter cake was measured using a NaI(Tl) scintillator (Crismatec™ , ORTEC DigiBASE) and recorded in MAESTRO ®-32 (Software Version 6.0, ORTEC). The source of radiation and the scintillator are mounted on a movable rack. The number of counts for the empty filter cell was measured for 10 min. The recording time was set to 30 s for the filtration of suspensions with additions of NaCl due to the short filtration time needed; the time was increased to 3 min for the suspension without the addition of ions. The absolute deviation of the solidosity was estimated as being ±0.02-0.05, with the error between individual measurements being lower than 0.03.

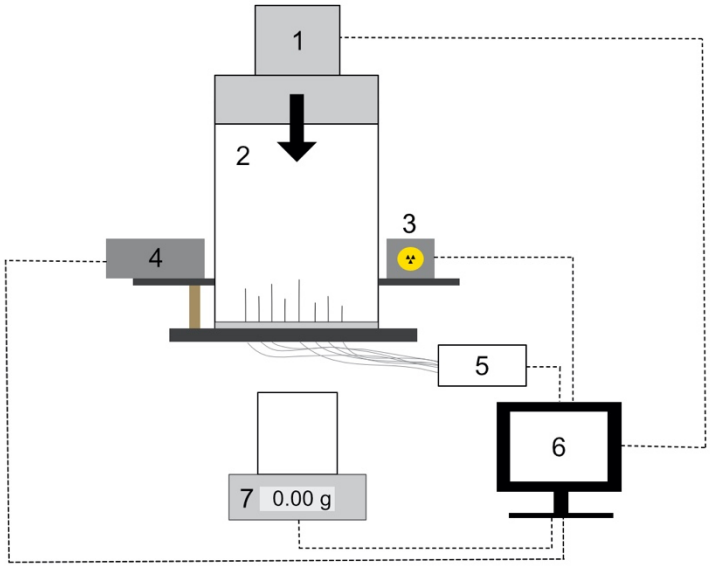

Figure 4.1 Schematic diagram of the filtration unit. 1: Piston press with its position recorded. 2: Plexiglas filter cell, with 8 pressure capillaries located at different heights. 3: ^{241}Am source of 10^9 Bq. 4: NaI(Tl) scintillator. 5: Pressure transducers. 6: Data acquisition unit. 7: Balance.

4.4.2 Electro-assisted filtration

The filtration set-up was modified [5] to allow for electro-assisted filtration, see Fig. 4.2. The metallic bottom plate and piston head are replaced by plastic materials. A supporting rack is added to the lower part of the filter cell (height of 0.03 m), thereby reducing the internal diameter to 0.05 m. Four pressure capillaries of perfluoroalkoxy alkene (PFA) are mounted through the bottom plate; these have circular holes of 0.6 mm located perpendicular to the flow at a distance from the filter medium of 2, 4, 6 and 8 mm, respectively.

Two electrodes, separated at a constant distance of 0.025 m, are connected to a DC power supply (EA-PSI 5299-02 A, Elektro-Automatik). The bottom electrode is comprised of a

platinum mesh (Unimesh 300) placed on the bottom plate, beneath the support filter and the filter medium; the upper electrode is comprised of a mesh (1x1 cm) of platinum wire of diameter 0.25 mm and is placed on the supporting rack inside the filter cell.

The temperature in the filter cell is measured by two PFA-coated K-type thermocouples placed at a distance of 5 and 30 mm, respectively, from the filter medium.

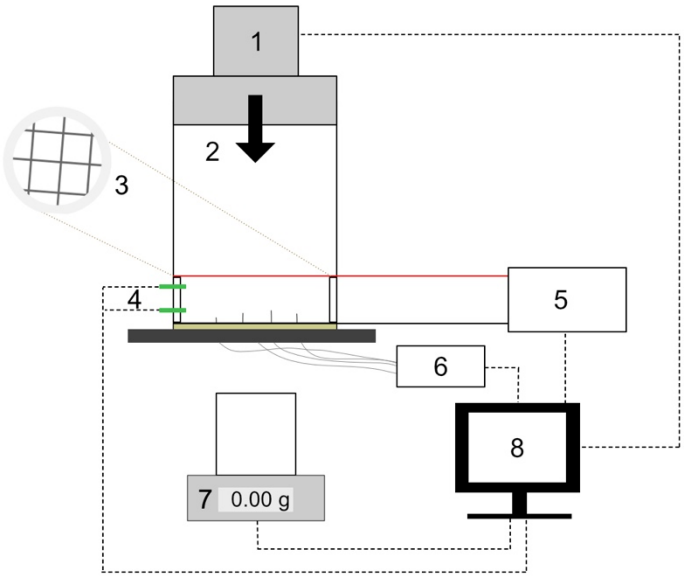

Figure 4.2. Schematic diagram of the filtration unit. 1: Piston press with its position recorded. 2: Plexiglas filter cell, with 4 pressure capillaries located at different heights. 3: Close up of anode mesh. 4: Thermocouples. 5: Power supply, current, voltage and power supply recorded. 6: Pressure transducers. 7: Balance. 8: Data acquisition unit.

4.5 Experimental conditions

4.5.1 Dead-end filtration of MCC

All experiments were performed at ambient temperature (i.e. 22 ºC) and with an applied filtration pressure of 3 bar. The filter medium used was a hydrophilic PES filter (Supor®, PALL Corps.) with a nominal pore size of 0.45 µm, according to the supplier. Grade 5 filter paper from Munktell Ahlstrom was used as an underlying support in addition to the PES filter medium.

4.5.2 Electro-assisted filtration of TEMPO-MFC

The electro-assisted filtration experiments were run at constant voltage, examining three levels: 6, 12 and 24 V/cm. The applied pressure was kept constant at 3 bar. In addition, dead-end filtration experiments were performed where no electric field was applied, as well as electro-osmotic dewatering where only an electric field of 24 V/cm was applied.

The filter medium used was a hydrophilic PES filter (Supor®, PALL Corporations) with a nominal pore size of 0.1 µm, according to the supplier. Grade 5 filter paper from Munktell Ahlstrom was used as an underlying support.

5

Results & Discussions

This chapter presents the main findings of the two papers appended in this thesis.

5.1 Dewatering MCC: The influence of ionic strength

Cellulose and ions interact in varying ways whilst cellulose-based products are being processed. It is a well-established fact that ionic strength plays an important role in controlling electrostatic interactions between the particles in the suspension, although the full extent of its effect on dead-end filtration of cellulose remains unknown. Thus, one aim of the present work was to investigate this using MCC as a model material for cellulose and NaCl to alter the ionic strength.

5.1.1 Characterisation of MCC

The SEM micrograph shown in Fig. 5.1 reveals aggregated structures of water-swollen MCC, of which most are somewhat cylindrical in shape. The particle size of the MCC was determined by laser diffraction, from which it was observed that 50 vol.% of the particles had an estimated particle diameter < 20.5 ± 0.9 μm. A specific surface area of 39 ± 2 m^2/g was obtained using nitrogen adsorption and the B.E.T. method; the particle size distribution and surface area are tabulated in Table 5.1. The carbohydrate composition of the MCC in question was 97% glucose, 1% mannose and 2% xylose, and its solid density was 1560 kg/m^3.

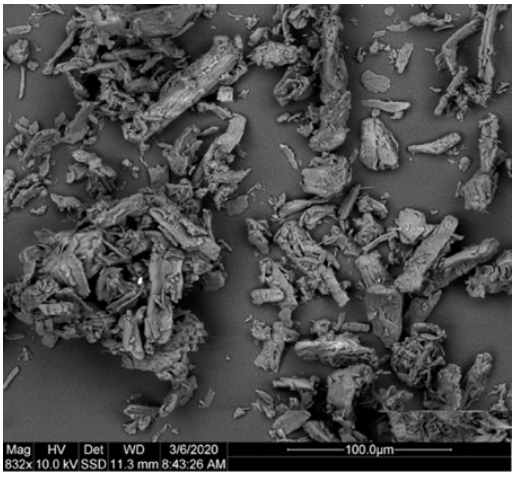

Figure 5.1 SEM micrograph of mechanically-treated MCC after the solvent-exchange procedure.

Table 5.1. Summary of particle size distribution in the mechanically treated plain suspension determined by laser diffraction and specific surface area measured by the B.E.T. method. The subscripts 10, 50 and 90 indicate that x vol.% of the particles are smaller than the value stated.

D_{10} [µm]	D_{50} [µm]	D_{90} [µm]	$A_{B.E.T.}$ [m^2/g]
8 ± 0.4	20.5 ± 0.9	45.7 ± 3	39 ± 2

To evaluate the influence of the ionic strength on the MCC suspension, the zeta potential (Fig. 5.2a) as well as particle/agglomerate size were determined. The absolute value of the zeta potential was observed to decrease with an increasing concentration of ionic strength: from 34.6 to 2.9 mV when 0.2 g/L NaCl was added. At ionic concentrations higher than 0.2 g/L, the effect was rather modest. A lower absolute value of the zeta potential indicates that the surface charges become more shielded as a consequence of the added ions, which can be explained by the EDL theory.

The findings from the zeta potential measurements agree with the results from the FBRM analysis (Fig. 5.2b); increasing the ionic strength led to an increased number of counts at a higher chord length, indicating the formation of MCC agglomerates. However, between 0.5-1 g/L NaCl, no significant difference can be observed, which is in line with the reported zeta potentials.

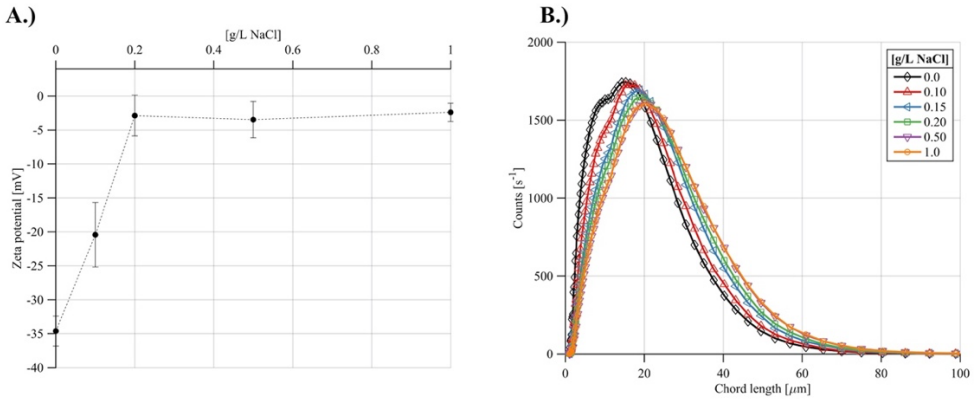

Figure 5.2 A.) Zeta potential vs. concentration of NaCl. B.) Counts (#/s) vs. chord length at varying concentrations of NaCl.

5.1.2 Dead-end filtration

Fig. 5.3 presents the filtrate volume obtained versus time for varying concentrations of NaCl. As can be seen, it is clear that increasing the ionic concentration causes an increased filtration rate. The reason behind the increased filtration rate when NaCl is added may be related to the agglomeration of MCC: upon agglomeration, the total surface area of the particles subjected to the liquid flow is reduced, there is less skin friction and the filtration resistance is thereby reduced. Once again, a minor difference is noticed between the two highest concentrations of NaCl: this could be partially explained by the FBRM results, which indicate that the particle/agglomerate size does not vary much between these two concentrations.

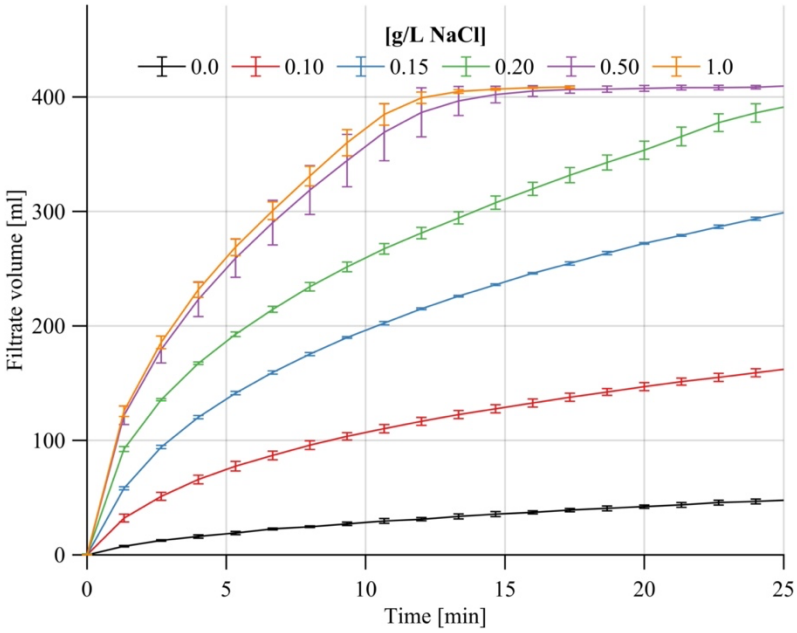

Figure 5.3 Filtrate volume vs. time at varying concentrations of NaCl.

A very low filtration rate was observed for the MCC suspension devoid of ions. This was associated with the probable formation of a highly resistant skin, as reported previously by Mattsson *et al.* [65], which may be related to particle-particle or particle-membrane interactions. The MCC particles in the suspension devoid of ions are hindered from forming agglomerates due to their negative surface charges (cf. zeta potential), so the initial layers of MCC particles deposited on the membrane may be densely compacted. Clogging of the filter medium, either internally or by various degrees of surface blocking, can also occur. However, the nominal pore size of the membrane is 0.45 µm, which is considerably smaller than the MCC particles and makes internal blocking unlikely. Nevertheless, the possibility of interactions occurring between the MCC particles and the filter medium is not rejected: partial surface blocking may have been the root cause of the formation of a skin.

Compressibility was evaluated by fitting the local data to the semi-empirical relations presented in Eqs. 3.15 and 3.16, see Fig 5.4 and Table 5.2. It is suggested, after classifying the model parameters according to the classification proposed in Table 3.1 (Ch. 3.1.3 Semi-empirical relations) [37], that the fitted parameters β and n in Table 5.2 correspond with high to moderate compressibility. No clear trends with respect to β can be observed, however, as the difference with respect to ionic concentration is rather modest. The values of n and α_0 indicate a slightly reduced compressibility with increasing ionic concentration in the range investigated. The

parameters of 0.1 g/L NaCl should nevertheless be interpreted with caution, as this data did not present a good fit.

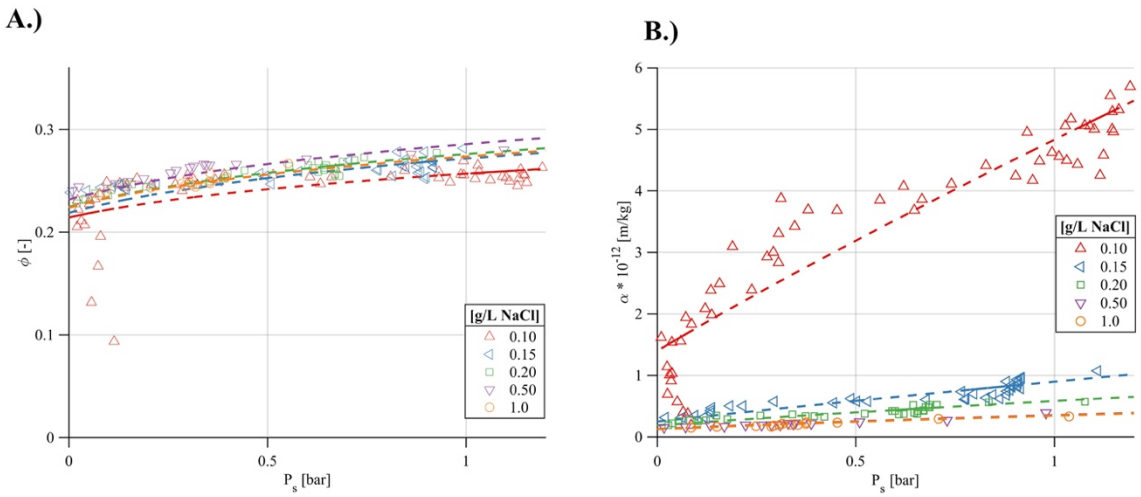

Figure 5.4. Fitting semi-empirical relations (Eqs. 3.15 and 3.16) to the experimental data. A.) Local solidosity vs. P_s B.) Local filtration resistance vs. P_s

Table 5.2 Model parameters obtained by fitting the local filtration data to Eqs. 3.15 and 3.16

[g/L NaCl]	φ_0 [-]	P_0 [kPa]	β [-]	$\alpha_0 * 10^{-11}$ [m/kg]	n [-]
0.10	0.21	31.6	0.13	14	0.87
0.15	0.22	31.6	0.15	2.5	0.89
0.20	0.23	31.6	0.15	1.9	0.79
0.50	0.23	31.6	0.15	1.3	0.69
1.0	0.23	31.6	0.14	1.3	0.71

A slightly different pressure dependency can be observed in Fig. 5.4 for the lowest concentration of NaCl: a more pronounced pressure dependency compared to the higher ionic concentrations. This may be related to the stability of the agglomerates formed and/or the distribution of particle/agglomerate size at the lower ionic concentrations. Surface charges that are not shielded as efficiently can result in the electrostatic repulsion between the particles remaining rather high, which can give rise to a different compactisation mechanism. Intricate details of the mechanism are, however, not yet fully understood.

In summary, the findings can be divided into three categories thus:

1. Suspensions devoid of ions: A high filtration resistance is observed. This may be related to the highly dense compactisation of the initial layers of particles deposited on the filter medium and/or partial surface blocking of the filter medium, the underlying cause of which remains to be established.

2. A concentration of 0.1 g/L NaCl: The MCC particles start to agglomerate, disturbing the formation of skin. The agglomerates formed are, however, rather weak. A higher pressure dependency is observed compared with the higher ionic concentrations.

3. Between 0.15-1 g/L NaCl: As the surface charges of the MCC become shielded more efficiently with increasing ionic concentration, the particles form agglomerates that continue to increase in size. This, in turn, leads to a reduction of the total surface area subjected to the liquid flow and the filtration resistance therefore decreases with increasing ionic concentration. At levels > 0.5 g/L NaCl, however, no clear difference is observed in terms of filtration rate, zeta potential and chord length distribution.

The findings of the study confirmed the importance of electrostatic interactions during the dead-end filtration of MCC, as identified previously by Mattsson *et. al* [38]. In their study, however, the electrostatic interactions were altered by adjusting the pH of the suspension: a reduction in pH caused the carboxylic acid groups present to protonate which, in turn, affected the surface charge of the MCC. In similarity with their study, an increased filtration rate was observed when the surface charges of the particles were more shielded efficiently, i.e. when ions were added.

5.2 Electro-assisted filtration of TEMPO-MFC

The challenging dewatering of microfibrillated cellulose impedes its commercialisation. Filtration, which is the most common mechanical dewatering method employed, is not a suitable option: the fibrils being subjected to the flow not only have a large surface area but also are long and flexible, allowing them to slide over each other to create a compact cake. Assisted filtration techniques may therefore be an appropriate way of enhancing dewatering. An example of such a technique is electro-assisted filtration, which was investigated in this work (Paper II). The experimental work is combined with molecular dynamics (MD) simulations to deepen understanding of the complicated dewatering mechanism on a molecular scale.

5.2.1 Characterisation

The pulp was oxidised successfully, as verified by a visible peak around 1603 cm^{-1} in the ATR-FTIR spectra, which confirms stretching of COO^- in the sodium form [66], see Fig. A1 in the Appendix. The carboxylate content of the TEMPO-MFC was 1.08 ± 0.02 mmol/g TEMPO-MFC, which is considerably higher than that of the unoxidised pulp (0.025 ± 0.002 mmol/g pulp). The introduction of carboxylate groups resulted in a negative zeta potential of 42.3 ± 1.5 mV.

SEM micrographs of the TEMPO-MFC revealed a highly fibrillated network, as presented in Fig. 5.5. The fibrillated material had a large surface area of 218 ± 12 m^2/g, determined by nitrogen adsorption after undergoing a solvent-exchange procedure. The B.E.T. surface area and other characteristics of the TEMPO-MFC are summarised in Table 5.3.

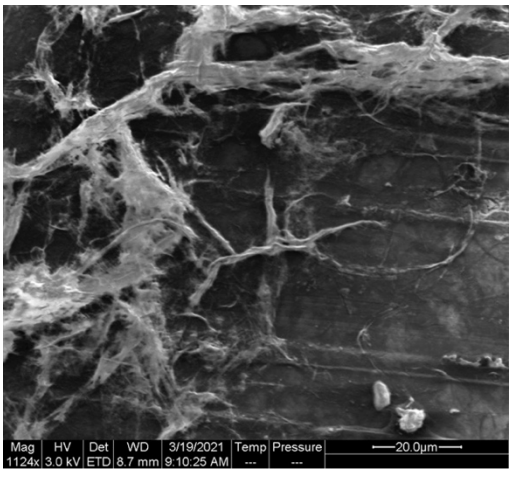

Figure 5.5 SEM micrograph of TEMPO-MFC.

Table 5.3 Summary of the characteristics of the TEMPO-MFC including zeta potential, carboxylate content and B.E.T. surface area.

Zeta potential [mV]	Carboxylate content [mmol/g TEMPO-MFC]	$A_{B.E.T.}$ [m^2/g]
-42.3 ± 1.5	1.08 ± 0.02	218 ± 12

5.2.2 Electro-assisted filtration

Figure 5.6 displays the dewatering rate versus time for cases in which only pressure (P), only an electric field (E) or a combination of the two (low (L), medium (M), and high (H)) were applied. It is apparent that more efficient dewatering is achieved by combining pressure with an electric field than using them separately. In addition, the dewatering rate is proportional to the strength of the electric field.

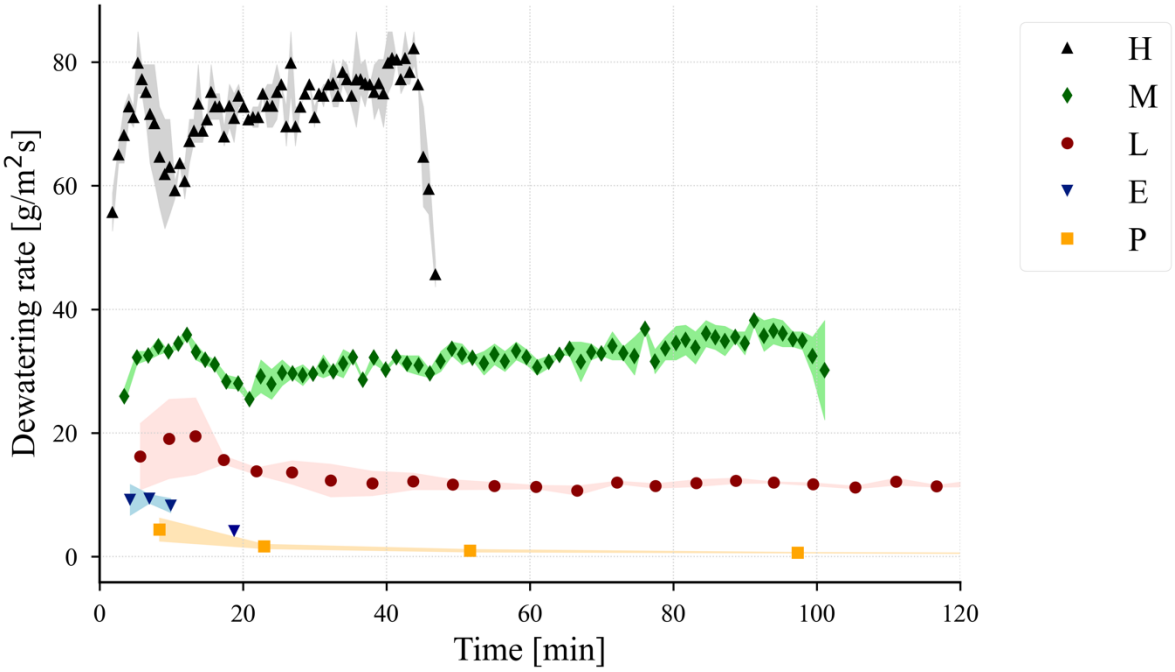

Figure 5.6 Dewatering rate vs. time, including standard deviation as shaded area from duplicate measurements. H= 24 V/cm, M= 12 V/cm, L = 6 V/cm, P= 0 V/cm; all with an applied pressure of 3 bar. E= 24 V/cm, but no applied pressure.

Electro-assisted filtration clearly improved dewatering of the suspension of TEMPO-MFC. The electrokinetic phenomena thereby introduced aid filtration by disturbing the formation of a resistant cake, whilst the electroosmotic flow of water enhances dewatering. In addition, ohmic heating results in a temperature rise (Fig. A2) which, in turn, reduces the viscosity of the liquid in the suspension [52] and aids dewatering. Furthermore, an interesting observation was made with regard to the dewatered structures formed: a channelled structure, which may provide good over-all permeability, see Figs. 5.7a and b, and was more pronounced at the two highest electric field strengths. A plausible explanation for this particular structure is that it stems, in part, from the electrophoretic movement of cellulose fibrils towards the anode. The design of the electrode creates an uneven electric field (see insert in Fig. 5.7c.), i.e. a localised electric field in connection with the anode wires, at which the TEMPO-MFC aggregate. Moreover, it is possible that the cellulose fibrils become aligned in this electric field, as has been reported in several studies [67–69]. In addition, the liquid flows through the square openings of the anode mesh, at which stage it drags along the TEMPO-MFC. The structure is then stabilised in pillars as a result of the electrophoretic movement of the fibrils towards the anode mesh and hypothetical alignment in the electric field. An example of a flow channel is indicated by a red arrow in Fig. 5.7b.

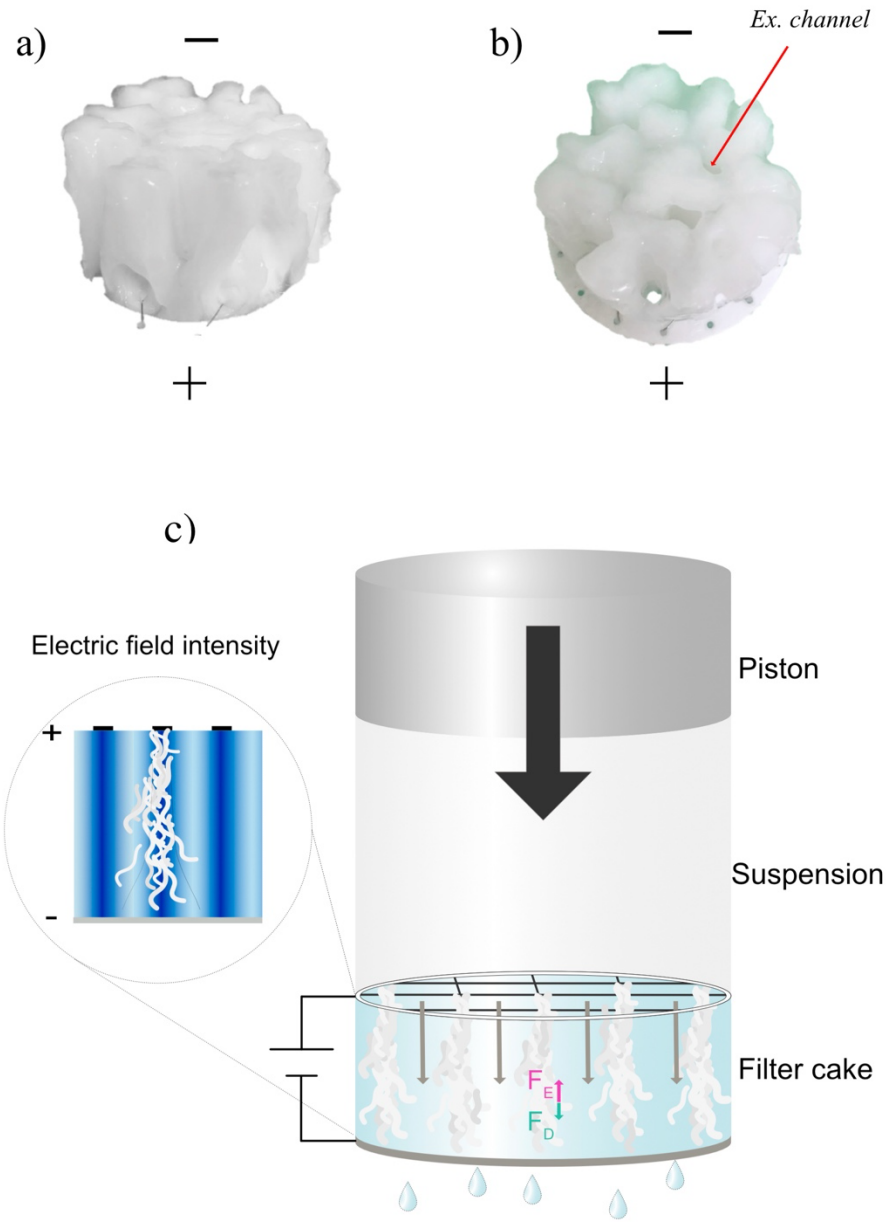

Figure 5.7 Top: Photographs of the structure formed at 12 V/cm and 3 bar with the locations of the electrodes (+ = anode; – = cathode). a.) frontal view and b.) overhead view, as seen from the cathode. Red arrow: example of a flow channel. c.) Schematic diagram of the suggested development of the channelled structures. Grey arrows: liquid flow through some of the square-openings. Pink arrow (F_E): electrophoretic force. Turquoise arrow (F_D): drag force on the TEMPO-MFC. Insert: close-up of the lower part of the filter cell, as seen from the front. The gradient shows the electric field: the darker colour, the higher its intensity.

Conventional dead-end filtration of the TEMPO-MFC suspension resulted in a very low filtration rate, with virtually non-existent dewatering early on (cf. Fig. 5.6), in agreement with Amini *et al.* [70]. One reason for the slow dewatering rate could be the large surface area of TEMPO-MFC being subjected to the liquid flow, possibly in combination with the formation of a highly dense skin at the filter medium (as discussed above for MCC).

When an electrical field alone was applied, however, dewatering stopped after a short period of time. Based on the current density profile presented in Fig. 5.8, a great electrical resistance appears to have developed in the system, which is apparent from the steep decline. The full reason behind the development of the said resistance is yet to be understood.

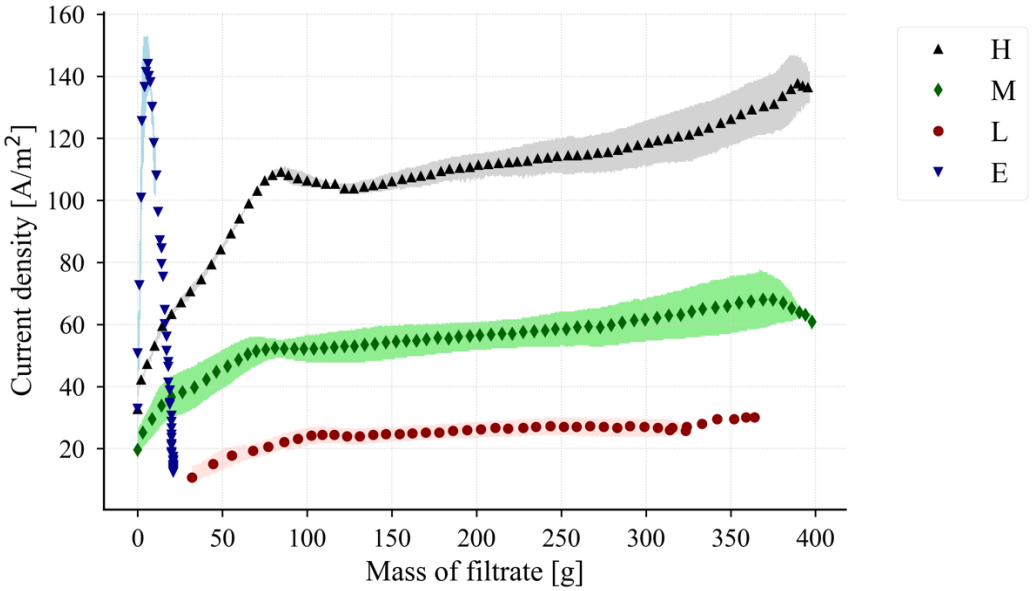

Figure 5.8 Current density vs. mass of filtrate, including standard deviation as shaded area from duplicate measurements. H= 24 V/cm, M= 12 V/cm, L = 6 V/cm; all with an applied pressure of 3 bar. E= 24 V/cm, but no applied pressure.

5.2.3 The dewatering mechanism

MD simulations were employed to study the dewatering mechanism at the molecular level: the velocity profile of interfibrillar water was studied and a simulation set-up that replicated a microscopic part of an electro-assisted dead-end filtration cell. Comprehensive details of the systems investigated are given in Paper II. The TEMPO-oxidised cellulose (TOC) oligomers used in the latter simulation set-up were modelled according to Fig. 5.9, where every other hydroxymethyl group is replaced by a carboxylate group.

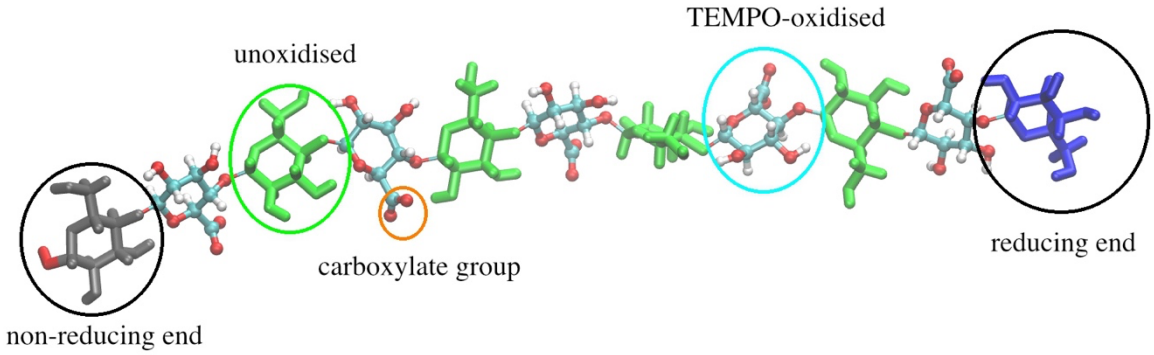

Figure 5.9 Model of TOC, where alternate hydroxymethyl groups are replaced by a carboxylate group.

5.2.3.1 Velocity profile of interfibrillar water

The electric field affects not only the fibrils but also the water in the system, since the cation movement towards the cathode causes water molecules to be transported in the same direction by hydrodynamic drag. This, in turn, improves dewatering. It is therefore interesting to observe the effect had by an electric field and/or pressure on interfibrillar water that will, upon leaving

the interfibrillar space, contribute to the free water in the system and may thus improve dewatering. The simulation set-up used is shown in Fig. 5.10a; the simulated pressure effect and/or electric field were applied in the positive x-direction.

The velocity profiles presented in Fig. 5.10b show a parabolic pressure profile typical for that of a Poiseuille flow: the maximum velocity is in the middle of the channel for the cases involving pressure, whereas the application of electric field alone showed a plug flow profile typical of electroosmotic flow. It should be noted that both pressure and electric field affect the water flow, but the effect of an electric field is significantly greater than that of pressure. Furthermore, the greatest maximum velocity in the cases investigated was caused by the combined effect of pressure and an electric field, and is therefore expected to contribute the most to the amount of free water in the system.

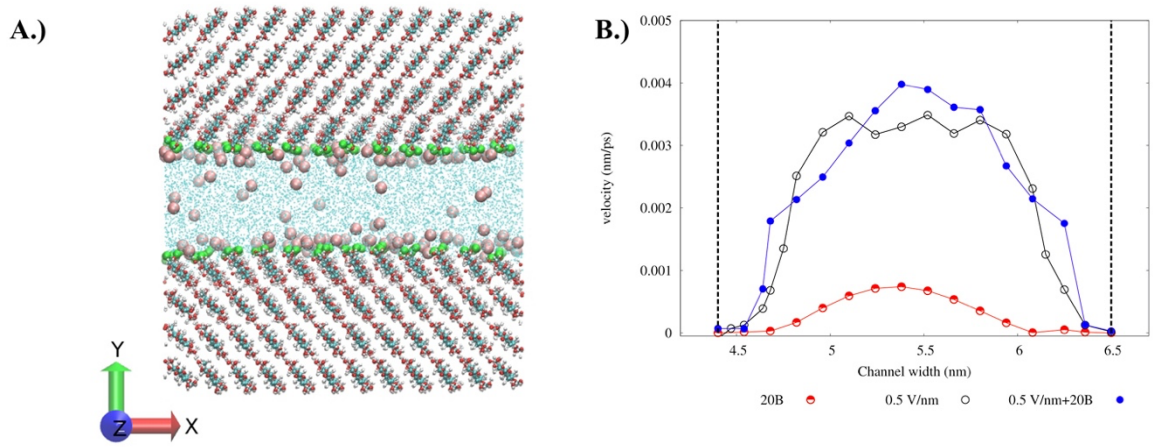

Figure 5.10 A.) Set-up used to study the flow of water trapped between the fibrils. The simulated pressure effect and/or electric field were applied in the positive x-direction. B.) Velocity profile of the water molecules trapped between the TOC fibrils. 20B corresponds to a simulated pressure effect of 20 bar.

5.2.3.2 Electro-assisted filtration

Finally, a simulation set-up was created that allowed for the simultaneous study of both the movement of fibrils and the flow of water molecules during electro-assisted filtration. A net simulated applied pressure effect was in the direction towards the filter medium and the electric field was applied in the same direction, see Fig. 5.11. It should, however, be stressed that this set-up is merely for studying the phenomena in a microscopic part of the filtration chamber for a time span of nanoseconds: it does not correspond to the experimental set-up used in the study because it would be impossible to include all of the time and length scales. Moreover, as it is impossible to account for the electrolysis reactions that occur at the electrodes, both the presence of a pH gradient and its associated consequences are not included. In addition, neither mechanical interlocking nor friction between the TOC fibrils was taken into account.

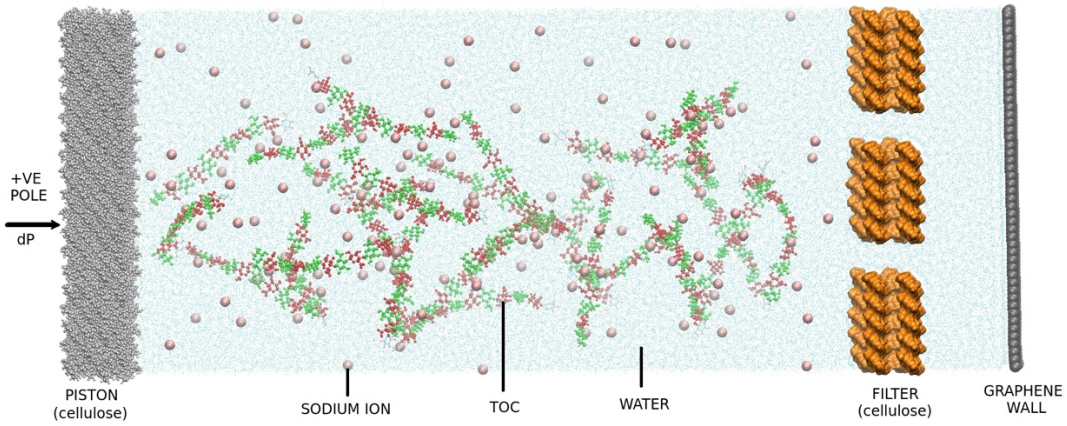

Figure 5.11 Schematic diagram of the set-up used to study electro-assisted dead-end filtration. A graphene wall is imposed on the filter end of the system to prevent water molecules from escaping and also to apply a negative pressure on the system, guaranteeing the filtration pressure desired. Pink spheres: sodium ions. Blue spheres: water molecules. Piston and filter medium: uncharged cellulose walls.

The dewatering rate (water molecules/ns) after 0.5 ns of filtration simulation is compared in Fig. 5.12a with solely applied pressure effect (10 and 20 bar), solely applied electric field (0.5 and 1 V/nm) and a combination of both. It is evident that a combination of an electric field and applied pressure results in the highest dewatering rate, as was also observed in the experimental results (cf. Fig. 5.6). Unfortunately, further comparisons cannot be made between the experimental and simulation results due to the limitations of the simulations stated previously.

Several reasons lie behind the improved dewatering rate resulting from electro-assisted filtration. One can be found in Fig. 5.12b, where the movement of negative TOC fibrils towards the anode under the effect of varying strengths of electric field can be observed: the stronger the electric field, the faster the movement. This means that the build-up of a flow-resistant filter cake is hindered. In addition, electroosmotic flow of water contributes to the enhanced dewatering rate and increases with increasing magnitude of electric field.

Another reason is that the interfibrillar water and cations are expelled more efficiently (cf. Fig. 5.10b), which contributes to the amount of free water in the system that can be removed upon the application of pressure and an electric field.

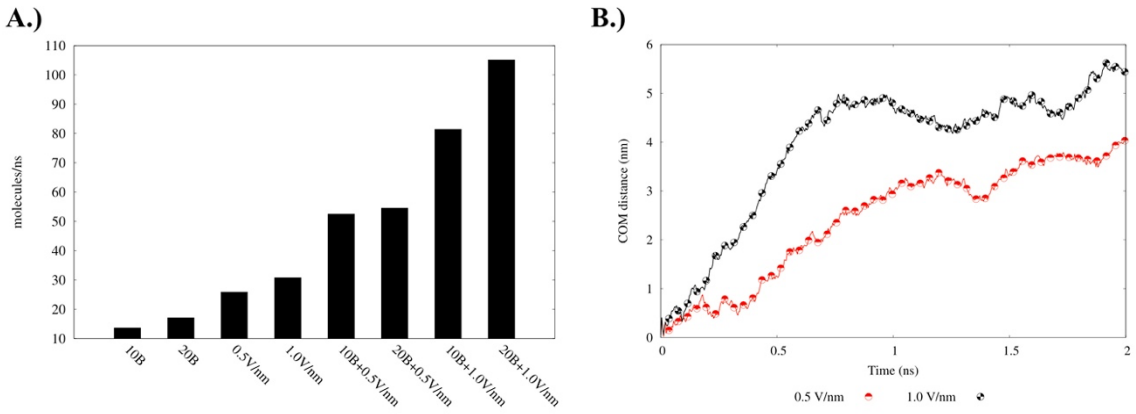

Figure 5.12 A.) Dewatering rate after 0.5 ns of simulation. B.) COM distance vs. time for electro-assisted filtration simulations with an applied pressure effect of 20 bar and an electric field of 0.5 V/nm (red) and 1 V/nm (black).

6

Conclusions and Future Work

This chapter presents the conclusions drawn from the two studies, along with suggestions for future work.

6.1 Conclusions

In this work, the dewatering of cellulose has been investigated in two studies employing a dead-end filtration technique to dewater microcrystalline cellulose at different ionic strengths and microfibrillated cellulose under the influence of an electric field. Although the two studies were based on cellulosic materials, it is difficult to draw any parallels between them due to differences related to the differing morphologies of the cellulosic material used. What can be concluded, however, is that filtration of the cellulosic materials investigated resulted in the occurrence of extensive filtration resistance when no modifications were made.

Regarding the dewatering of MCC, it was found that the addition of ions shielded the surface charges of the MCC particles and promoted agglomeration which, in turn, affected the filtration rate since the total surface area subjected to the liquid flow was reduced. Ionic strength was shown to be a highly influential parameter during the filtration of MCC: both the local and the average filtration resistance decreased as the ionic strength increased from 0-1 g/L NaCl. The influence was not linear: the largest change in terms of agglomerate size or filtration properties was in the lower concentration range (0-0.2 g NaCl/L): at the higher end (0.5-1 g NaCl/L), almost no noticeable differences were observed. The findings indicated that electrostatic interactions play an important role during the dead-end filtration of MCC, which is in agreement with earlier study by Mattsson *et al.* [38] where the electrostatic interactions were altered via changes in pH.

Electro-assisted filtration was found to be an efficient method for improving the dewatering of TEMPO-MFC. Dewatering was very slow when only pressure was applied but, upon the application of electric field, it was greatly enhanced due to the electrokinetic phenomena thereby introduced. Furthermore, a channelled structure, with a high overall degree of permeability, was formed, which may also have contributed positively to the improvement in dewatering.

Experimental as well as simulation results implied that a combination of an electric field and pressure was necessary to dewater the MFC suspension efficiently. It should be noted, however, that further comparisons between the experimental and simulation results cannot be made here: the time and length scales vary, and the MD simulations have certain limitations, including the electrolysis reactions not being accounted for, as well as mechanical interlocking and friction between the fibrils.

The simulation results suggest that the improved dewatering rate during electro-assisted filtration may be due to electroosmotic flow of water as well as electrophoretic movement of the fibril towards the anode, which may counteract the build-up of a filter cake and thereby reduce resistance to filtration. The MD simulations suggest another reason for the improved dewatering rate: interfibrillar water may be expelled more efficiently upon the application of both an electric field and pressure. This, in turn, contributes to the bulk water in the system which can be separated more easily from the suspension by either pressure or an electric field.

6.2 Future work

Much remains to be uncovered on the subject of the electro-assisted filtration of MFC and nanocellulose in general. Future research should, for example, focus on the impact of the channelled structure that was observed forming during the electro-assisted filtration of TEMPO-MFC in more detail. The further study of electroosmotic dewatering of MFC, i.e. applying only an electric field and without additional mechanical pressure, would also be of great interest.

Acknowledgments

The financial aid received from the Swedish Research Council (*Vetenskapsrådet*) is gratefully acknowledged. In addition, this thesis would not have been possible without the support of the following people, whom I wish to thank sincerely:

- Prof. Hans Theliander – you have inspired me ever since I was a Master's student, nourishing my interest not in only the wonders of pulp and paper but also filtration. Your expertise is invaluable!

- Dr Nabin Karna – for our interesting talks, inspiring quotes and the valuable exchange of knowledge.

- Associate professor Tuve Mattsson –for all your assistance and discussions in the execution of the first paper.

- All my colleagues at SIKT: Ph.D. students, post-docs, research engineers, administrators and inline manager – yes, it has been a strange year indeed, but we did our best and coped with it.

- Esa and Torbjörn in the workshop –for your skilful work with the filtration set-up.

- The professors, TAs and students involved in KAA060 Transport Phenomena - for making teaching such a fun experience.

- Mrs. Maureen Sondell – for your professional language review.

- Mr. Anders Ahlbom –for fruitful discussions during the slow days in the home office.

As is the custom, I would like to express my deepest gratitude to my nearest and dearest. Thank you, my siblings, for your support, even though you don't always understand what I do, and thank you, my parents for encouraging me in your own special ways.

Most of all, I wish to thank you, Oscar, my soon-to-be husband. You make me smile at the end of each day, even on those when I fail in the lab.

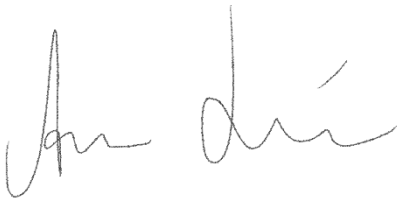

Göteborg, 18 August 2021

Bibliography

[1] T. Li, C. Chen, A.H. Brozena, J.Y. Zhu, L. Xu, C. Driemeier, J. Dai, O.J. Rojas, A. Isogai, L. Wågberg, L. Hu, Developing fibrillated cellulose as a sustainable technological material, Nature. 590 (2021) 47–56. https://doi.org/10.1038/s41586-020-03167-7.

[2] Y. Peng, D.J. Gardner, Y. Han, Drying cellulose nanofibrils: in search of a suitable method, Cellulose. 19 (2012) 91–102. https://doi.org/10.1007/s10570-011-9630-z.

[3] S. Sinquefield, P.N. Ciesielski, K. Li, D.J. Gardner, S. Ozcan, Nanocellulose Dewatering and Drying: Current State and Future Perspectives, ACS Sustainable Chem. Eng. 8 (2020) 9601–9615. https://doi.org/10.1021/acssuschemeng.0c01797.

[4] J. Wetterling, S. Jonsson, T. Mattsson, H. Theliander, The Influence of Ionic Strength on the Electroassisted Filtration of Microcrystalline Cellulose, Ind. Eng. Chem. Res. 56 (2017) 12789–12798. https://doi.org/10.1021/acs.iecr.7b03575.

[5] J. Wetterling, T. Mattsson, H. Theliander, Local filtration properties of microcrystalline cellulose : Influence of an electric field, Chemical Engineering Science. 171 (2017) 368–378. https://doi.org/10.1016/j.ces.2017.05.054.

[6] I. Heiskanen, K. Backfolk, A. Kotilainen, V. Gaidelis, J. Sidaravicius, Process for treating microfibrillated cellulose and microfibrillated cellulose treated according to the process, US20140088301A1, 2014. https://patents.google.com/patent/US20140088301A1/en (accessed June 3, 2021).

[7] J. Wetterling, K. Sahlin, T. Mattsson, G. Westman, H. Theliander, Electroosmotic dewatering of cellulose nanocrystals, Cellulose. 25 (2018) 2321–2329. https://doi.org/10.1007/s10570-018-1733-3.

[8] M. Ek, G. Gellerstedt, G. Henriksson, Wood Chemistry and Wood Biotechnology, De Gruyter, Inc., Berlin/Boston, GERMANY, 2009. http://ebookcentral.proquest.com/lib/chalmers/detail.action?docID=476006 (accessed April 20, 2021).

[9] H. Meier, Chemical and morphological aspects of the fine structure of wood, Pure and Applied Chemistry. 5 (1962) 37–52. https://doi.org/10.1351/pac196205010037.

[10] T. Saito, S. Kimura, Y. Nishiyama, A. Isogai, Cellulose Nanofibers Prepared by TEMPO-Mediated Oxidation of Native Cellulose, Biomacromolecules. 8 (2007) 2485–2491. https://doi.org/10.1021/bm0703970.

[11] A.N. Fernandes, L.H. Thomas, C.M. Altaner, P. Callow, V.T. Forsyth, D.C. Apperley, C.J. Kennedy, M.C. Jarvis, Nanostructure of cellulose microfibrils in spruce wood, PNAS. 108 (2011) E1195–E1203. https://doi.org/10.1073/pnas.1108942108.

[12] T. Dumitrică, Intrinsic twist in Iβ cellulose microfibrils by tight-binding objective boundary calculations, Carbohydrate Polymers. 230 (2020) 115624. https://doi.org/10.1016/j.carbpol.2019.115624.

[13] E. Sjöström, Chapter 1 - THE STRUCTURE OF WOOD, in: E. Sjöström (Ed.), Wood Chemistry (Second Edition), Academic Press, San Diego, 1993: pp. 1–20. https://doi.org/10.1016/B978-0-08-092589-9.50005-X.

[14] C.-L. Huang, H. Lindström, R. Nakada, J. Ralston, Cell wall structure and wood properties determined by acoustics—a selective review, Holz Roh Werkst. 61 (2003) 321–335. https://doi.org/10.1007/s00107-003-0398-1.

[15] H. Kangas, P. Lahtinen, A. Sneck, A.-M. Saariaho, O. Laitinen, E. Hellén, Characterization of fibrillated celluloses. A short review and evaluation of characteristics with a combination of methods, Nordic Pulp & Paper Research Journal. 29 (2014) 129–143. https://doi.org/10.3183/npprj-2014-29-01-p129-143.

[16] M.A. Hubbe, P. Tayeb, M. Joyce, P. Tyagi, M. Kehoe, K. Dimic-Misic, L. Pal, Rheology of Nanocellulose-rich Aqueous Suspensions: A Review, (2017) 106.
[17] L. Wågberg, G. Decher, M. Norgren, T. Lindström, M. Ankerfors, K. Axnäs, The Build-Up of Polyelectrolyte Multilayers of Microfibrillated Cellulose and Cationic Polyelectrolytes, Langmuir. 24 (2008) 784–795. https://doi.org/10.1021/la702481v.
[18] M. Ghanadpour, F. Carosio, P.T. Larsson, L. Wågberg, Phosphorylated Cellulose Nanofibrils: A Renewable Nanomaterial for the Preparation of Intrinsically Flame-Retardant Materials, Biomacromolecules. 16 (2015) 3399–3410. https://doi.org/10.1021/acs.biomac.5b01117.
[19] T. Saito, A. Isogai, TEMPO-Mediated Oxidation of Native Cellulose. The Effect of Oxidation Conditions on Chemical and Crystal Structures of the Water-Insoluble Fractions, Biomacromolecules. 5 (2004) 1983–1989. https://doi.org/10.1021/bm0497769.
[20] M. Pääkkö, M. Ankerfors, H. Kosonen, A. Nykänen, S. Ahola, M. Österberg, J. Ruokolainen, J. Laine, P.T. Larsson, O. Ikkala, T. Lindström, Enzymatic Hydrolysis Combined with Mechanical Shearing and High-Pressure Homogenization for Nanoscale Cellulose Fibrils and Strong Gels, Biomacromolecules. 8 (2007) 1934–1941. https://doi.org/10.1021/bm061215p.
[21] A.F. Turbak, F.W. Snyder, K.R. Sandberg, Microfibrillated cellulose, a new cellulose product: properties, uses, and commercial potential, J. Appl. Polym. Sci.: Appl. Polym. Symp.; (United States). 37 (1983). https://www.osti.gov/biblio/5062478.
[22] F.W. Herrick, R.L. Casebier, J.K. Hamilton, K.R. Sandberg, Microfibrillated cellulose: morphology and accessibility, J. Appl. Polym. Sci.: Appl. Polym. Symp.; (United States). 37 (1983). https://www.osti.gov/biblio/5039044.
[23] D. Klemm, F. Kramer, S. Moritz, T. Lindström, M. Ankerfors, D. Gray, A. Dorris, Nanocelluloses: A New Family of Nature-Based Materials, Angewandte Chemie International Edition. 50 (2011) 5438–5466. https://doi.org/10.1002/anie.201001273.
[24] L. Wågberg, L. Winter, L. Ödberg, T. Lindström, On the charge stoichiometry upon adsorption of a cationic polyelectrolyte on cellulosic materials, Colloids and Surfaces. 27 (1987) 163–173. https://doi.org/10.1016/0166-6622(87)80335-9.
[25] T Lindström, L Winter, Mikrofibrillär cellulosa som komponent vid papperstillverkning, STFI-meddelande C159, 1988.
[26] A. Isogai, T. Saito, H. Fukuzumi, TEMPO-oxidized cellulose nanofibers, Nanoscale. 3 (2011) 71–85. https://doi.org/10.1039/C0NR00583E.
[27] G. Thoorens, F. Krier, E. Rozet, B. Carlin, B. Evrard, Understanding the impact of microcrystalline cellulose physicochemical properties on tabletability, International Journal of Pharmaceutics. 490 (2015) 47–54. https://doi.org/10.1016/j.ijpharm.2015.05.026.
[28] F.M. Tiller, S. Haynes Jr., W.-M. Lu, The role of porosity in filtration VII effect of side-wall friction in compression-permeability cells, AIChE Journal. 18 (1972) 13–20. https://doi.org/10.1002/aic.690180104.
[29] H. Darcy, Les fontaines publiques de la ville de Dijon : exposition et application des principes à suivre et des formules à employer dans les questions de distribution d'eau... / par Henry Darcy,..., (1856) 659.
[30] B.F. Ruth, Studies in Filtration III. Derivation of General Filtration Equations, Ind. Eng. Chem. 27 (1935) 708–723. https://doi.org/10.1021/ie50306a024.
[31] G.H. Meeten, A dissection method for analysing filter cakes, Chemical Engineering Science. 48 (1993) 2391–2398. https://doi.org/10.1016/0009-2509(93)81060-9.

[32] H. Saveyn, D. Curvers, L. Pel, P. De Bondt, P. Van der Meeren, In situ determination of solidosity profiles during activated sludge electrodewatering, Water Research. 40 (2006) 2135–2142. https://doi.org/10.1016/j.watres.2006.04.003.
[33] M. Shirato, T. Aragaki, K. Ichimura, N. Ootsuji, Porosity Variation in Filter Cake Under Constant-Pressure Filtration, Journal of Chemical Engineering of Japan. 4 (1971) 172–177. https://doi.org/10.1252/jcej.4.172.
[34] C. Johansson, H. Theliander, Measuring concentration and pressure profiles in deadend filtration, Filtration. 3 (2003) 114–120.
[35] M. Shirato, M. Sambuichi, H. Kato, T. Aragaki, Internal flow mechanism in filter cakes, AIChE Journal. 15 (1969) 405–409. https://doi.org/10.1002/aic.690150320.
[36] F.M. Tiller, W.F. Leu, Basic data fitting in filtration, J. Chinese Institute Chemical Engineers,. 11 (1980) 61–70.
[37] W.F. Leu, Cake filtration, University of Houston, 1981.
[38] T. Mattsson, M. Sedin, H. Theliander, On the local filtration properties of microcrystalline cellulose during dead-end filtration, Chemical Engineering Science. 72 (2012) 51–60. https://doi.org/10.1016/j.ces.2012.01.022.
[39] E. Sjöström, The origin of charge on cellulosic fibers, Nordic Pulp & Paper Research Journal. 4 (1989) 90–93. https://doi.org/10.3183/npprj-1989-04-02-p090-093.
[40] B.F. Ruth, Correlating Filtration Theory with Industrial Practice., Ind. Eng. Chem. 38 (1946) 564–571. https://doi.org/10.1021/ie50438a010.
[41] R.S. Faibish, M. Elimelech, Y. Cohen, Effect of Interparticle Electrostatic Double Layer Interactions on Permeate Flux Decline in Crossflow Membrane Filtration of Colloidal Suspensions: An Experimental Investigation, Journal of Colloid and Interface Science. 204 (1998) 77–86. https://doi.org/10.1006/jcis.1998.5563.
[42] R.M.T. Sanchez, Filtration as a method of isoelectric point (IEP) determination, Materials Chemistry and Physics. 26 (1990) 173–180. https://doi.org/10.1016/0254-0584(90)90036-A.
[43] T. Mattsson, J. Durruty, J. Wetterling, H. Theliander, The influence of ionic strength on the local filtration properties of titanium dioxide, Filtration. 15 (2015) 48–57.
[44] K. Sim, J. Lee, H. Lee, H.J. Youn, Flocculation behavior of cellulose nanofibrils under different salt conditions and its impact on network strength and dewatering ability, Cellulose. 22 (2015) 3689–3700. https://doi.org/10.1007/s10570-015-0784-y.
[45] B.F. Ruth, Correlating Filtration Theory with Industrial Practice., Ind. Eng. Chem. 38 (1946) 564–571. https://doi.org/10.1021/ie50438a010.
[46] H. Saveyn, P. Van der Meeren, G. Pauwels, R. Timmerman, Bench- and pilot-scale sludge electrodewatering in a diaphragm filter press, Water Science and Technology. 54 (2006) 53–60. https://doi.org/10.2166/wst.2006.725.
[47] A. Mahmoud, J. Olivier, J. Vaxelaire, A.F.A. Hoadley, Electro-dewatering of wastewater sludge: Influence of the operating conditions and their interactions effects, Water Research. 45 (2011) 2795–2810. https://doi.org/10.1016/j.watres.2011.02.029.
[48] J.Q. Shang, K.Y. Lo, Electrokinetic dewatering of a phosphate clay, Journal of Hazardous Materials. 55 (1997) 117–133. https://doi.org/10.1016/S0304-3894(97)00018-6.
[49] A.K. Vijh, Electrochemical Aspects of Electroosmotic Dewatering of Clay Suspensions, Drying Technology. 13 (1995) 215–224. https://doi.org/10.1080/07373939508916950.
[50] R. Hofmann, C. Posten, Improvement of dead-end filtration of biopolymers with pressure electrofiltration, Chemical Engineering Science. 58 (2003) 3847–3858. https://doi.org/10.1016/S0009-2509(03)00271-9.

[51] G. Gözke, F. Kirschhöfer, S. Heissler, M. Trutnau, G. Brenner-Weiss, J. Ondruschka, U. Obst, C. Posten, Filtration kinetics of chitosan separation by electrofiltration, Biotechnology Journal. 7 (2012) 262–274. https://doi.org/10.1002/biot.201000466.
[52] K. Weber, W. Stahl, Improvement of filtration kinetics by pressure electrofiltration, Separation and Purification Technology. 26 (2002) 69–80. https://doi.org/10.1016/S1383-5866(01)00118-6.
[53] S.P. Moulik, Physical aspects of electrofiltration, Environ. Sci. Technol. 5 (1971) 771–776. https://doi.org/10.1021/es60056a001.
[54] S. Wall, The history of electrokinetic phenomena, Current Opinion in Colloid & Interface Science. 15 (2010) 119–124. https://doi.org/10.1016/j.cocis.2009.12.005.
[55] M. Citeau, O. Larue, E. Vorobiev, Influence of Filter Cell Configuration and Process Parameters on the Electro-Osmotic Dewatering of Sewage Sludge, Separation Science and Technology. 47 (2012) 11–21. https://doi.org/10.1080/01496395.2011.616567.
[56] N.C. Lockhart, Electroosmotic dewatering of clays. I. Influence of voltage, Colloids and Surfaces. 6 (1983) 229–238. https://doi.org/10.1016/0166-6622(83)80015-8.
[57] P.-A. Tuan, V. Jurate, S. Mika, Electro-Dewatering of Sludge Under Pressure and Non-Pressure Conditions, Environmental Technology. 29 (2008) 1075–1084. https://doi.org/10.1080/09593330802180294.
[58] A.A.A. Aziz, D.R. Dixon, S.P. Usher, P.J. Scales, Electrically enhanced dewatering (EED) of particulate suspensions, Colloids and Surfaces A: Physicochemical and Engineering Aspects. 290 (2006) 194–205. https://doi.org/10.1016/j.colsurfa.2006.05.020.
[59] O. Larue, E. Vorobiev, Sedimentation and water electrolysis effects in electrofiltration of kaolin suspension, AIChE Journal. 50 (2004) 3120–3133. https://doi.org/10.1002/aic.10227.
[60] J. Olivier, J.-B. Conrardy, A. Mahmoud, J. Vaxelaire, Electro-dewatering of wastewater sludge: An investigation of the relationship between filtrate flow rate and electric current, Water Research. 82 (2015) 66–77. https://doi.org/10.1016/j.watres.2015.04.006.
[61] O. Theander, E.A. Westerlund, Studies on dietary fiber. 3. Improved procedures for analysis of dietary fiber, J. Agric. Food Chem. 34 (1986) 330–336. https://doi.org/10.1021/jf00068a045.
[62] A. Mautner, F. Mayer, M. Hervy, K.-Y. Lee, A. Bismarck, Better together: synergy in nanocellulose blends, Phil. Trans. R. Soc. A. 376 (2018) 20170043. https://doi.org/10.1098/rsta.2017.0043.
[63] E.J. Foster, R.J. Moon, U.P. Agarwal, M.J. Bortner, J. Bras, S. Camarero-Espinosa, K.J. Chan, M.J.D. Clift, E.D. Cranston, S.J. Eichhorn, D.M. Fox, W.Y. Hamad, L. Heux, B. Jean, M. Korey, W. Nieh, K.J. Ong, M.S. Reid, S. Renneckar, R. Roberts, J.A. Shatkin, J. Simonsen, K. Stinson-Bagby, N. Wanasekara, J. Youngblood, Current characterization methods for cellulose nanomaterials, Chem. Soc. Rev. 47 (2018) 2609–2679. https://doi.org/10.1039/C6CS00895J.
[64] X. Wang, T. Maloney, H. Paulapuro, Internal Fibrillation in Never-dried and Once-dried Chemical Pulps, Appita Journal. 56 (2003) 455–459.
[65] T. Mattsson, M. Sedin, H. Theliander, Filtration properties and skin formation of micro-crystalline cellulose, Sep. Purif. Technol. 96 (2012) 139–146. https://doi.org/10.1016/j.seppur.2012.05.029.
[66] A. Onyianta, M. Dorris, R. Williams, Aqueous morpholine pre-treatment in cellulose nanofibril (CNF) production: comparison with carboxymethylation and TEMPO oxidisation pre-treatment methods, Cellulose. 25 (2018) 1–18. https://doi.org/10.1007/s10570-017-1631-0.

[67] H.C. Kim, J.W. Kim, L. Zhai, J. Kim, Strong and tough long cellulose fibers made by aligning cellulose nanofibers under magnetic and electric fields, Cellulose. 26 (2019) 5821–5829. https://doi.org/10.1007/s10570-019-02496-9.
[68] D. Bordel, J.-L. Putaux, L. Heux, Orientation of Native Cellulose in an Electric Field, Langmuir. 22 (2006) 4899–4901. https://doi.org/10.1021/la0600402.
[69] H.G. Wise, H. Takana, F. Ohuchi, A.B. Dichiara, Field-Assisted Alignment of Cellulose Nanofibrils in a Continuous Flow-Focusing System, ACS Appl. Mater. Interfaces. 12 (2020) 28568–28575. https://doi.org/10.1021/acsami.0c07272.
[70] E. (Nima) Amini, M. Tajvidi, D.W. Bousfield, D.J. Gardner, S.M. Shaler, Dewatering Behavior of a Wood-Cellulose Nanofibril Particulate System, Scientific Reports. 9 (2019) 14584. https://doi.org/10.1038/s41598-019-51177-x.

Appendix

ATR-FTIR spectra

The spectra presented in Fig. A1 show the following peaks, in addition to COO^- stretching in the sodium form at around 1603 cm^{-1} (red dashed line): C-O stretching at around 1020 cm^{-1} (orange dashed line), C-H stretching at around 2880 cm^{-1} (green dashed line) and O-H stretching at around 3330 cm^{-1} (pink dashed line).

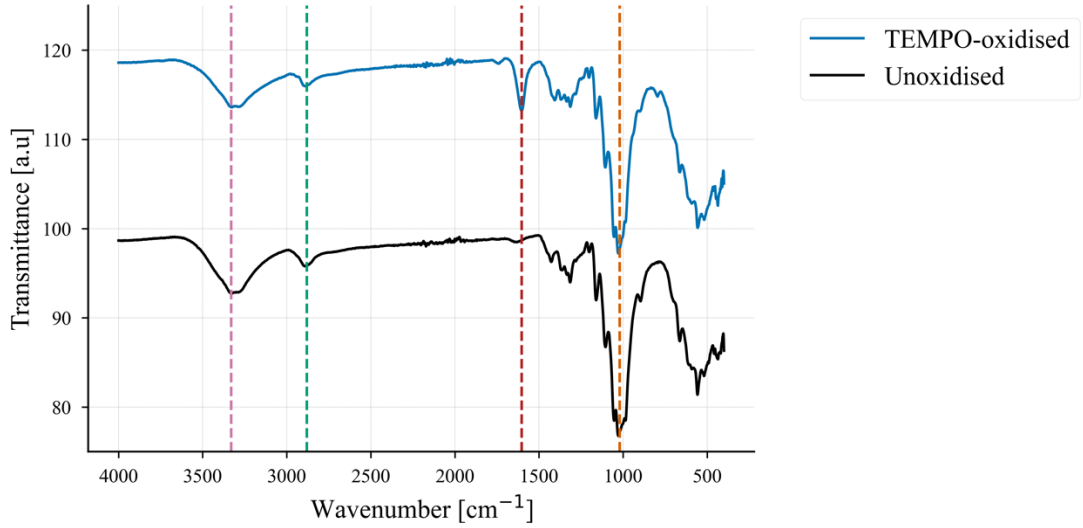

Figure A1 Overlapping ATR-FTIR spectra from TEMPO-oxidised (blue) and unoxidised (black) pulp. The dashed lines correspond to the stretching of various functional groups, where pink = OH, green = CH, red = COO^- and orange = CO.

Electro-assisted filtration

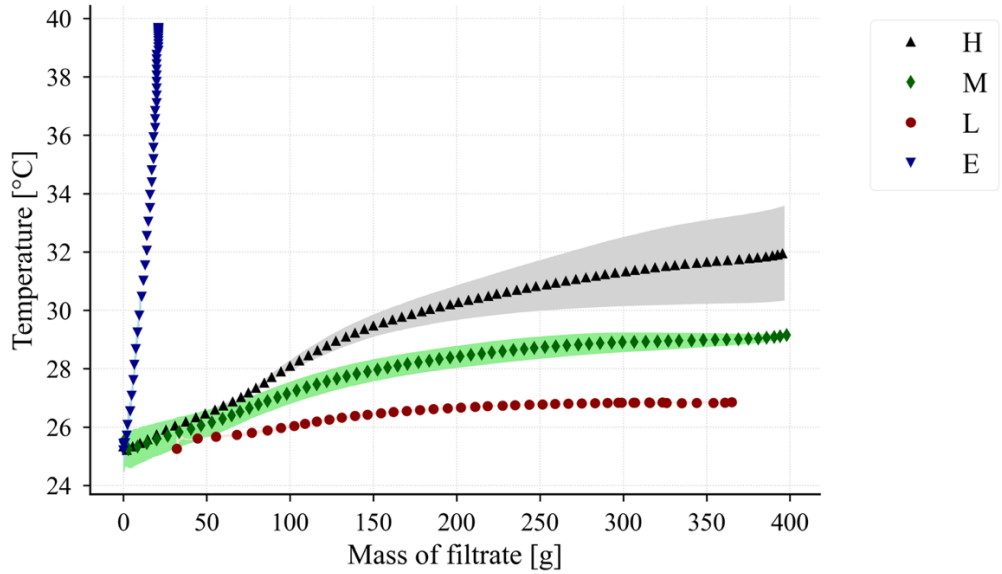

Figure A2 Temperature measured 5 mm from the filter medium. H= 24 V/cm, M= 12 V/cm, L = 6 V/cm, all with an applied pressure of 3 bar. E= 24 V/cm but with no applied pressure.